



Dynamic modeling and control of a 6-DOF micro-vibration simulator



Jianfeng Yang^{a, b}, Zhenbang Xu^{a, *}, Qingwen Wu^a, Mingchao Zhu^a, Shuai He^a, Chao Qin^a

^aInnovation Lab of Space Robot System, Changchun Institute of Optics, Fine Mechanics and Physics, Chinese Academy of Sciences, No. 3888 Dong Nanhu Road, Changchun 130033, China

^bUniversity of Chinese Academy of Sciences, No. 19A Yuquan Road, Beijing 100049, China

ARTICLE INFO

Article history:

Received 23 November 2015

Received in revised form 15 June 2016

Accepted 15 June 2016

Available online 28 June 2016

Keywords:

Parallel manipulator

Micro-vibrations

Simulator

Optical payload

ABSTRACT

A micro-vibration simulator with multiple degrees of freedom is required for performance testing of sensitive instruments in a micro-vibration environment on-board spacecraft before launch. In this study, a novel 6-DOF micro-vibration simulator (6-MVS) is proposed, which can reproduce a micro-vibration environment with a wide bandwidth of disturbance frequencies. The complete inverse dynamic equations of the proposed 6-MVS are derived using the Kane method, which is very suitable for processing by computer. The validity of the derived dynamic equations is then verified by co-simulation. The structural performance of the 6-MVS is investigated using the finite element method. Based on this dynamic model, a robust proportional-integral (PI) control scheme is then performed. The control performance of the proposed controller is evaluated by co-simulation. The analysis and simulation results show that the proposed robust PI controller has excellent robustness and stability and the 6-MVS can exactly produce the required micro-vibration spectrum.

© 2016 Elsevier Ltd. All rights reserved.

1. Introduction

There is an increasing requirement for precision pointing and extreme stability for current and forthcoming optical remote sensors, which have a larger aperture and a higher resolution imaging. The James Webb space telescope [1], terrestrial planet finder [2] and Space Interferometry Mission [3] are such examples where microarcsecond pointing and nanometer levels of motion stability are required. However, micro-vibrations generated by on-board motion equipment in spacecraft (for example, reaction/momentum wheel assemblies (R/MWA), cryo-coolers, thrusters, solar array drive mechanisms, etc.) can greatly degrade the performance of optical payloads with high pointing accuracy and stability [4].

Since micro-vibrations have characteristics of low amplitude, a wide frequency range, and multiple directions, current shake tables are unable to reproduce the required micro-vibration environment. Hostens et al. [5, 6] have proposed a six degree-of-freedom (DOF) vibration simulator, which can be used to generate high-amplitude and narrow-band vibrations. Park et al. [7] have developed a multiple-degree-of-freedom micro-vibration emulator to test jitter in spacecrafts, which can generate the disturbance spectrum of flight RWAs. However, this device has some coupling effects causing differences between the target input and the measured data responses along different axes. For space payloads, ground experiments are essential before launch, including image quality testing of the optical system in the micro-vibration environment. However, no suitable micro-vibration

* Corresponding author.

E-mail addresses: yangjeff2013@163.com (J. Yang), xuzhenbang@gmail.com (Z. Xu), wuqw@ciomp.ac.cn (Q. Wu), mingchaozhu@gmail.com (M. Zhu), xiaoxiao4032@126.com (S. He), qinchaojlu@163.com (C. Qin).

simulator exists that is qualified for this work. The usual solution is to adopt the actual disturbance resources or use dummy resources in the ground experiments. The R/MWA is generally regarded as one of the largest disturbance sources onboard a spacecraft [8]. Therefore, a real R/MWA is usually used for the micro-vibration test. However, it is uncommon to use all the flight R/MWAs to conduct the ground validating experiments because of scheduling issues or product assurance activities. Therefore, development of a micro-vibration shaking platform, which can replace the real flight R/MWAs, is considered to be an important adjunct to the development processes for space missions.

Parallel manipulators such as the Gough-Stewart platform (GSP) have been recently employed in various applications, because they have the advantages of high maneuverability, precision, high stiffness, and a large payload driven capability compared with serial manipulators. Li and Xu [9] have presented a three-prismatic-revolute-cylindrical parallel kinematic machine, and have investigated its dynamic modeling and robust control. A six degree-of-freedom parallel kinematic machine has been developed by Dong et al. [10], which is used for the motion simulation of hazardous chemical transportation. The Gough-Stewart platform, also known as the hexapod, is one of the most widely used parallel manipulators [11–15] and its kinematics, dynamics and control problems have been studied by many researchers. Oftadeh et al. [16] have presented explicit dynamics formulation for the GSP and utilized the Lagrange method to verify the resulting dynamics equations. Dasgupta and Mruthyunjaya [17] have derived an inverse dynamic formulation using the Newton-Euler approach for the GSP, with frictional forces occurring in the joints; the mass of inertia of the pods was also taken into consideration in their study. Staicu [18, 19] has developed a recursive matrix approach in kinematics and dynamics modeling of parallel robots, which can reduce the number of equations and computation operations significantly. Jiang et al. [20–24] have investigated an optimal design of the GSP with dynamic isotropy, as well as the influence of passive joint damping. Behrouz et al. [25] have developed a full parameter model of the GSP damped vibrations, which includes parametric expressions of the damped eigenfrequencies and the corresponding eigenvectors.

The control strategies for the parallel manipulator can be divided into two categories: control in the joint space and control in the task space [26]. The former control scheme can be readily employed in industry, but does not always guarantee high performance for parallel manipulators [27]. Kim et al. [28] have proposed a robust nonlinear control scheme in the joint space for an electro-hydraulic parallel manipulator based on the Lyapunov redesign method, but coupling is not taken into account, which should not be ignored for high performance tracking controllers. Wu et al. [29] presented an improved robust nonlinear controller, which is composed of the linear control part, nonlinear part and excitation compliment part. This proposed controller has the advantages of fine adjustability, low power consumption and a wide frequency range of isolation in all directions. But its pivotal objective is to attenuate the micro-vibrations. Superior control performance can potentially be provided using the control scheme in the task space. Han et al. have published a series of reports on robust controls for 6-DOF parallel manipulators, which include a computed force and velocity control, proportional plus derivative control and decoupling control schemes, etc. [30–34]. Kim et al. [35] have proposed a robust nonlinear task space control with a friction estimator for a dynamoelectric GSP. However, most studies have focused mainly on displacement or velocity trajectory tracking control, while acceleration trajectory tracking control of a parallel manipulator with multiple degrees of freedom is still rare. Although some acceleration trajectory control strategies have been reported in Refs. [36, 37], they are only suitable for shake tables with a single degree of freedom.

In this study, a 6-DOF micro-vibration simulator (6-MVS) has been developed, which can reproduce micro-vibrations with different amplitudes and frequencies. While a conventional GSP has stretched rods, the structural configuration of the proposed 6-MVS has been improved and has rods of fixed length. Since the mass of the rods in a conventional GSP is relatively heavy, a GSP may have low and closely-spaced local natural frequencies [38]. As a result, the natural frequencies of the overall system are reduced. The improved configuration simulator that is presented in this study can solve this problem, and its structural characteristics have been analyzed using the finite element method (FEM). Moreover, flexure joints are adopted to avoid non-linear effects due to friction, backlash, and micro-impacts which are produced by traditional joints with bearings. The inverse dynamics models, which consider the effect of the flexure joints, were established using the Kane method. A co-simulation was

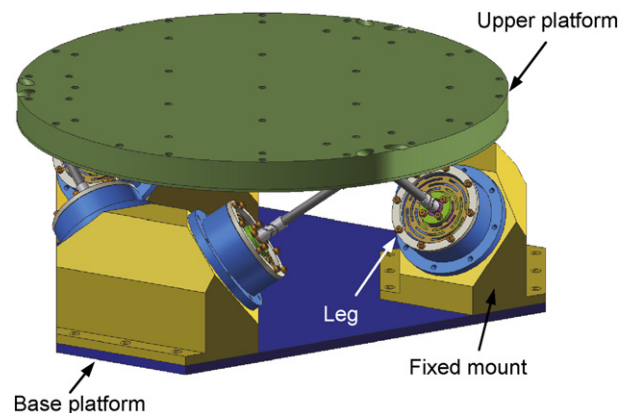


Fig. 1. Virtual prototype of the 6-DOF micro-vibration simulator.

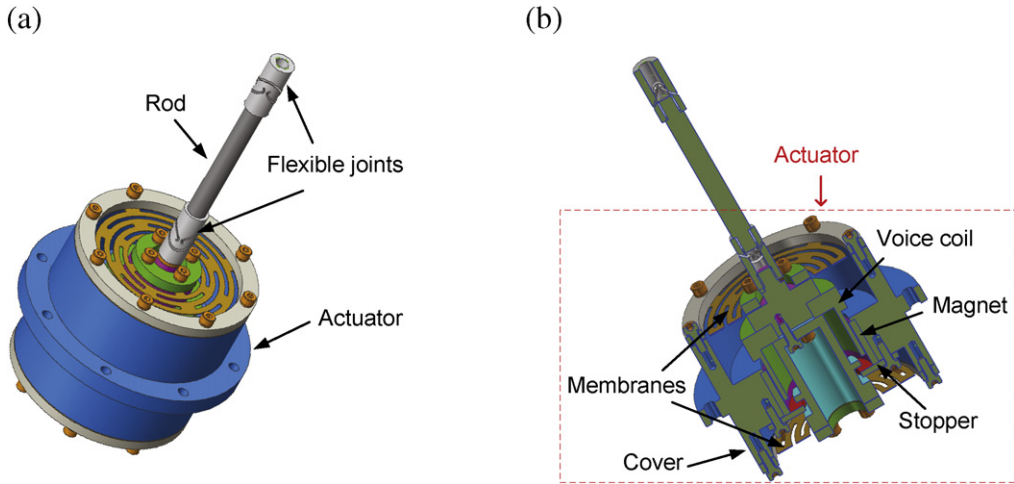


Fig. 2. 3-D model of the leg: (a) isometric view and (b) cross-sectional view.

then adopted to verify the validity of the dynamics models, which combined ADAMS with MATLAB/Simulink. Finally, a robust proportional-integral (PI) controller based on the inverse dynamics model was designed. This control strategy was designed for the acceleration control of the parallel manipulator, which considered the effects of uncertainties such as modeling errors, unknown loads, and parameter measurements. Its performance was analyzed in theory and simulation, including stability, precision and robustness of the proposed controller.

2. Mechanical structure

A virtual prototype of the 6-DOF micro-vibration simulator is shown in Fig. 1. The 6-MVS consists of an upper platform, a base platform, three fixed mounts and six identical legs. The detailed structure of the leg is depicted in Fig. 2, which includes an actuator, a rod and two flexure joints. The actuator is attached to a fixed mounting by bolts. A permanent magnet is fixed to the cover of the actuator, and a voice coil is connected to the cover by two membranes. The two membranes perform the function of a spring, for axial compliance only. One flexure joint is used to connect the voice coil motor to the rod, which is made of carbon fiber, and the other joint is used to connect the actuator to the upper platform. This design can reduce the sprung mass attached to the membrane and increase the bending frequency of the single actuator [38, 39].

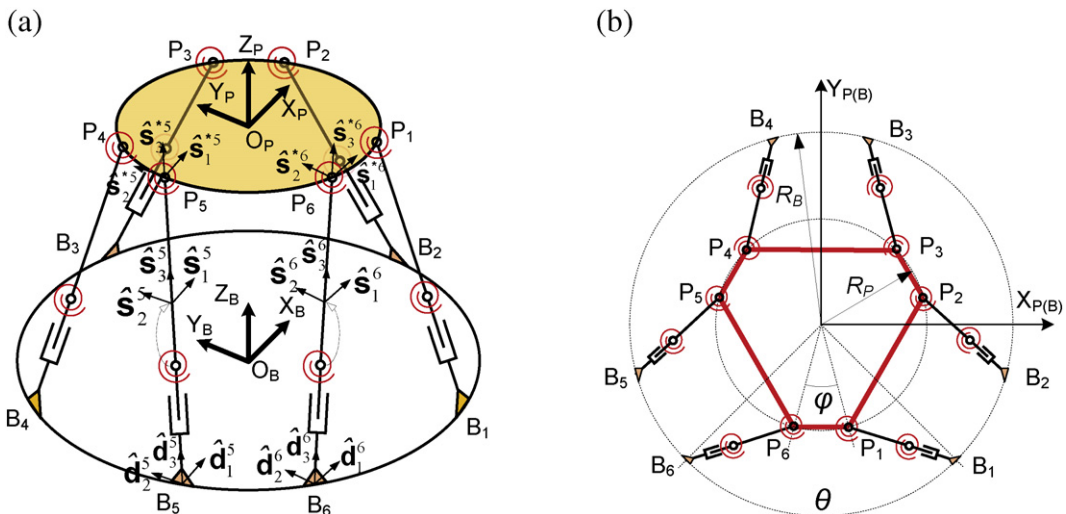


Fig. 3. A schematic view of the 6-DOF micro-vibration simulator: (a) isometric view and (b) vertical view.

3. Dynamic model

Nomenclature	
${}^B_P\mathbf{R}$	rotation matrix of transformation from the body frame {P} to the base frame {B}
$\mathbf{J}_{pi,q}$	Jacobian matrix relating the general velocity to the velocity of the upper flexure joint
$\mathbf{J}_{d,q}$	Jacobian matrix relating the general velocity to the sliding velocity of the actuator
\mathbf{E}_3	unit 3×3 matrix
α, β, γ	X-Y-Z fixed angles
$Q_1^{si}, Q_2^{si}, Q_1^{pi}, Q_2^{pi}, Q_3^{pi}$	Z-Y-X Euler angles of successive rotation
$\hat{\mathbf{s}}_3^i, \hat{\mathbf{d}}_3^i$	unit vectors along the i^{th} rod and actuator, respectively
s_i, d_i	lengths of the i^{th} rod and actuator, respectively
${}^P\mathbf{p}_c$	position vector of the centroid of upper platform under the body frame {P}
\mathbf{t}	translational vector (position of upper platform)
$\boldsymbol{\omega}$	angular velocity of upper platform
$\boldsymbol{\omega}_{si}, \boldsymbol{\epsilon}_{si}$	angular velocity and acceleration of the i^{th} rod, respectively
$\boldsymbol{\omega}^{pi}$	angular velocity of the i^{th} rod with respect to the upper platform
$d_i, \dot{d}_i, \ddot{d}_i$	length, sliding velocity and acceleration of the i^{th} actuator, respectively
$\mathbf{a}_{di}^c, \mathbf{a}_{si}^c$	accelerations of the i^{th} actuator and rod, respectively
m_p, m_{si}, m_{di}	masses of the upper platform, rod and actuator, respectively
${}^P\mathbf{I}_c$	inertia matrix of upper platform under the body frame {P}
${}^B\mathbf{I}_{si}$	inertia matrix of the i^{th} rod under the body frame {B}
k_1^i, k_2^i	torsional stiffness coefficients of the i^{th} lower flexure joint
k_1^i, k_2^i, k_3^i	torsional stiffness coefficients of the i^{th} upper flexure joint
$\mathbf{F}_D, \mathbf{M}_D$	external force and moment
$\mathbf{M}_1^i, \mathbf{M}_2^i$	elastic moments of the i^{th} lower flexure and upper flexure, respectively
F_{di}	exciting force of the i^{th} actuator

The scheme of the 6-DOF vibration simulator is shown in Fig. 3. The {P} coordinate system refers to the body frame fixed to the geometric center of the upper flexure joints, while the {B} coordinate system refers to the base frame attached to the geometric center of the fixed mounts. The linear motions are denoted as surge (x), sway (y), and heave (z) along the $X_B - Y_B - Z_B$ axes of the base frame. The angles of the upper platform around the X_B, Y_B, Z_B axes are the angular motions roll (γ), pitch (β), and yaw (α). The upper flexure joint points on the upper platform are given by ${}^P\mathbf{p}_i$ in frame {P} and the fixed mounts on the base platform by ${}^B\mathbf{b}_i$ in frame {B}, where the pre-superscripts B and P denote the base frame and the body frame, respectively. R_p and R_B describe the radii of the upper and base platforms. The angle between P_6 and P_1 is denoted by φ . As illustrated in Fig. 3 (b), the angle between B_6 and B_1 is denoted by θ . Frame $\hat{\mathbf{d}}^i$ is the reference frame which is attached to the base platform at $B_i (i = 1 \dots 6)$ with $\hat{\mathbf{d}}_3^i$ along the i^{th} actuator. The hat (^) above the variables indicates that it is a unit of length. The $\hat{\mathbf{s}}^i$ coordinate system is located on the i^{th} rod at the center of mass of the lower flexure joint with $\hat{\mathbf{s}}_3^i$ along the i^{th} rod. The $\hat{\mathbf{s}}^{si}$ coordinate system is fixed to the upper platform and its original point coincides with P_i . $\hat{\mathbf{s}}_3^{si}$ denotes the installation direction of the i^{th} upper flexure joint.

3.1. Generalized speeds

As shown in Fig. 4, the i^{th} flexure joint P_i with respect to the base frame {B} can be described by:

$$\mathbf{l}_{pi} = \mathbf{t} + {}^B_P\mathbf{R} \cdot {}^P\mathbf{p}_i \tag{1}$$

where \mathbf{t} is the position vector of the body frame, $\mathbf{t} = [x, y, z]^T$ and the rotation matrix of the transformation from the body frame {P} to the base frame {B} is ${}^B_P\mathbf{R}$, which adopts X-Y-Z fixed angles. The rotation matrix is given by:

$${}^B_P\mathbf{R} = \begin{bmatrix} \cos \alpha \cos \beta & \cos \alpha \sin \beta \sin \gamma - \sin \alpha \cos \gamma & \cos \alpha \sin \beta \cos \gamma + \sin \alpha \sin \gamma \\ \sin \alpha \cos \beta & \sin \alpha \sin \beta \sin \gamma + \cos \alpha \cos \gamma & \sin \alpha \sin \beta \cos \gamma - \cos \alpha \sin \gamma \\ -\sin \beta & \cos \beta \sin \gamma & \cos \beta \cos \gamma \end{bmatrix} \tag{2}$$

Taking the derivative of Eq. (1) with respect to time, the velocity mapping function can be obtained as:

$$\mathbf{v}_{pi} = \dot{\mathbf{l}}_{pi} = \dot{\mathbf{t}} + \boldsymbol{\omega} \times ({}^B_P\mathbf{R} \cdot {}^P\mathbf{p}_i) = \left[\mathbf{E}_3, {}^B_P\mathbf{R} ({}^P\dot{\mathbf{p}}_i) {}^T_P\mathbf{R}^T \right] \dot{\mathbf{q}} \tag{3}$$

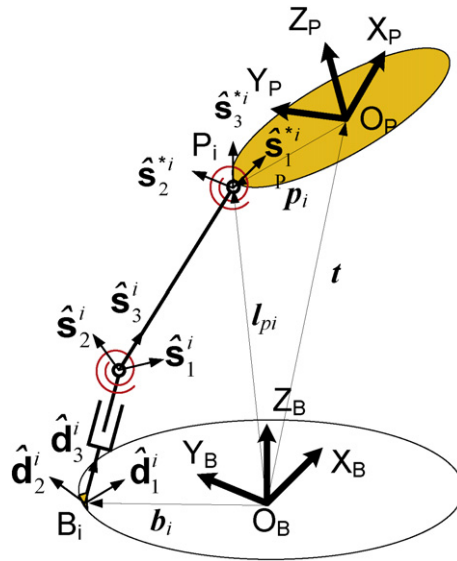


Fig. 4. Kinematic diagram of the i^{th} leg.

where \mathbf{v}_{p_i} is the velocity of the upper flexure joint P_i , $\dot{\mathbf{t}}$ and $\boldsymbol{\omega}$ are the translational velocity and angular velocity of the upper platform, respectively, $\dot{\mathbf{t}} = [\dot{x}, \dot{y}, \dot{z}]^T$, and $\boldsymbol{\omega} = [\dot{\gamma}, \dot{\beta}, \dot{\alpha}]^T$, \mathbf{E}_3 is a unit 3×3 matrix, ${}^P\tilde{\mathbf{p}}_i$ is the skew symmetry matrix of ${}^P\mathbf{p}_i$, $\dot{\mathbf{q}}$ is the general velocity of the upper platform, and Eq. (3) can be rewritten as:

$$\mathbf{v}_{p_i} = \mathbf{J}_{p_i, \mathbf{q}} \cdot \dot{\mathbf{q}} \tag{4}$$

where $\mathbf{J}_{p_i, \mathbf{q}}$ denotes a Jacobian matrix relating the general velocity to the velocity of the upper flexure joint, $\mathbf{J}_{p_i, \mathbf{q}} = \begin{bmatrix} \mathbf{E}_3, {}^B\mathbf{R}({}^P\tilde{\mathbf{p}}_i)^T {}^B\mathbf{R}^T \end{bmatrix}$.

Similarly, the acceleration of the upper flexure joint P_i can be obtained as:

$$\mathbf{a}_{p_i} = \ddot{\mathbf{t}} + \dot{\boldsymbol{\omega}} \times {}^B\mathbf{p}_i + \boldsymbol{\omega} \times (\boldsymbol{\omega} \times {}^B\mathbf{p}_i) \tag{5}$$

where ${}^B\mathbf{p}_i = {}^B\mathbf{R} \cdot {}^P\mathbf{p}_i$.

The velocity and acceleration of the centroid of the upper platform are given by:

$$\mathbf{v}_c = \dot{\mathbf{t}} + \boldsymbol{\omega} \times ({}^B\mathbf{R} \cdot {}^P\rho_c) \tag{6}$$

$$\mathbf{a}_c = \ddot{\mathbf{t}} + {}^B\mathbf{R} \cdot {}^P\tilde{\rho}_c^T \cdot {}^B\mathbf{R}^T \dot{\boldsymbol{\omega}} + \dot{\boldsymbol{\omega}}^2 ({}^B\mathbf{R} \cdot {}^P\rho_c) \tag{7}$$

where ${}^P\rho_c$ denotes the position vector of the centroid of the upper platform under the body frame $\{P\}$, and ${}^P\tilde{\rho}_c$ and $\dot{\boldsymbol{\omega}}$ are the skew symmetric matrices of ${}^P\rho_c$ and $\boldsymbol{\omega}$, respectively.

$$\mathbf{l}_{BP}^i = \mathbf{t} + {}^B\mathbf{p}_i - \mathbf{b}_i \tag{8}$$

The vector of the i^{th} rod in the frame $\{B\}$ can be described by:

$$s_i \hat{\mathbf{s}}_3^i = \mathbf{l}_{BP}^i - d_i \hat{\mathbf{d}}_3^i \tag{9}$$

where s_i and d_i denote the length of the i^{th} rod and actuator, respectively.

Dot-multiplying both sides of Eq. (9) by $s_i \hat{\mathbf{s}}_3^i$ gives:

$$s_i^2 = (\mathbf{l}_{BP}^i - d_i \hat{\mathbf{d}}_3^i)^T \cdot (\mathbf{l}_{BP}^i - d_i \hat{\mathbf{d}}_3^i) = l_{BP}^{i2} - 2d_i \hat{\mathbf{d}}_3^{iT} \mathbf{l}_{BP}^i + d_i^2 \tag{10}$$

Simplifying Eq. (10) yields:

$$d_i^2 - 2d_i \hat{\mathbf{d}}_3^T \mathbf{l}_{BP}^i + l_{BP}^i{}^2 - s_i^2 = 0 \tag{11}$$

Solving Eq. (11), the length d_i of the rod can be obtained as:

$$d_i = \hat{\mathbf{d}}_3^T \mathbf{l}_{BP}^i - \sqrt{\left(\hat{\mathbf{d}}_3^T \mathbf{l}_{BP}^i\right)^2 - l_{BP}^i{}^2 + s_i^2} \tag{12}$$

Taking the derivative of both sides of Eq. (10) with respect to time, and simplifying, the sliding velocity of the actuator can be described by:

$$\dot{d}_i = \left(\mathbf{l}_{BP}^i - d_i \hat{\mathbf{d}}_3\right)^T \left(\mathbf{J}_{pi,q} \dot{\mathbf{q}}\right) / \left[\left(\mathbf{l}_{BP}^i - d_i \hat{\mathbf{d}}_3\right)^T \hat{\mathbf{d}}_3\right] \tag{13}$$

To obtain the sliding acceleration of the actuator, the time derivative of Eq. (13) can be taken to yield:

$$\ddot{d}_i = \left(\mathbf{J}_{pi,q} \dot{\mathbf{q}} - \dot{d}_i \hat{\mathbf{d}}_3\right)^T \left(\mathbf{J}_{pi,q} \dot{\mathbf{q}} - \dot{d}_i \hat{\mathbf{d}}_3\right) + \left(\mathbf{l}_{BP}^i - d_i \hat{\mathbf{d}}_3\right)^T \mathbf{a}_{pi} / \left[\left(\mathbf{l}_{BP}^i - d_i \hat{\mathbf{d}}_3\right)^T \hat{\mathbf{d}}_3\right] \tag{14}$$

Based on their physical meaning, the velocities of the upper flexure joint P_i can also be described in terms of the velocity of the centroid of the actuator and the angular velocity of the rod under frame {B} as:

$$\mathbf{v}_{pi} = \dot{d}_i \hat{\mathbf{d}}_3 + \boldsymbol{\omega}_{si} \times \left(s_i \hat{\mathbf{s}}_3\right) \tag{15}$$

Taking the cross-product of the above equation with $\hat{\mathbf{s}}_3$ yields:

$$\hat{\mathbf{s}}_3 \times \mathbf{v}_{pi} = \hat{\mathbf{s}}_3 \times \left(\dot{d}_i \hat{\mathbf{d}}_3\right) + \hat{\mathbf{s}}_3 \times \left[\boldsymbol{\omega}_{si} \times \left(s_i \hat{\mathbf{s}}_3\right)\right] \tag{16}$$

Considering the assumption that rotation is not allowed about the rod axis (i.e. $\boldsymbol{\omega}_{si}^T \cdot \hat{\mathbf{s}}_3 = 0$) and simplifying Eq. (16), the angular velocity of the i^{th} rod can be obtained by:

$$\boldsymbol{\omega}_{si} = \frac{\hat{\mathbf{s}}_3 \times \mathbf{v}_{pi} - \dot{d}_i \hat{\mathbf{s}}_3 \times \hat{\mathbf{d}}_3}{s_i} \tag{17}$$

The angular velocity of the i^{th} rod with respect to the upper platform can be described as:

$$\boldsymbol{\omega}_{pi} = \boldsymbol{\omega} - \boldsymbol{\omega}_{si} \tag{18}$$

Taking the derivative of both sides of Eq. (17) with respect to time, the angular acceleration of the rod can be described by:

$$\boldsymbol{\varepsilon}_{si} = \frac{\boldsymbol{\omega}_{si} \times \hat{\mathbf{s}}_3 \times \mathbf{v}_{pi} + \hat{\mathbf{s}}_3 \times \mathbf{a}_{pi} - \left[\dot{d}_i \hat{\mathbf{s}}_3 \times \hat{\mathbf{d}}_3 + \dot{d}_i \left(\boldsymbol{\omega}_{si} \times \hat{\mathbf{s}}_3\right) \times \hat{\mathbf{d}}_3\right]}{s_i} \tag{19}$$

The velocity of the centroid of the i^{th} actuator and rod can be written as:

$$\mathbf{v}_{c,di} = \dot{\mathbf{l}}_{c,di} = \dot{d}_i \hat{\mathbf{d}}_3 \tag{20}$$

$$\mathbf{v}_{c,si} = \dot{d}_i \hat{\mathbf{d}}_3 + \frac{1}{2} s_i \boldsymbol{\omega}_{si} \times \hat{\mathbf{s}}_3 \tag{21}$$

According to Eqs. (3) and (15), the following expression can be obtained:

$$s_i \boldsymbol{\omega}_{si} \times \hat{\mathbf{s}}_3 = \dot{\mathbf{t}} + \boldsymbol{\omega} \times {}^B \mathbf{p}_i - \dot{d}_i \hat{\mathbf{d}}_3 \tag{22}$$

Substituting Eq. (22) into Eq. (21) yields:

$$\mathbf{v}_{c,si} = \dot{d}_i \hat{\mathbf{d}}_3 + \frac{1}{2} \left(\dot{\mathbf{t}} + \boldsymbol{\omega} \times {}^B \mathbf{p}_i - \dot{d}_i \hat{\mathbf{d}}_3\right) = \frac{1}{2} \left(\dot{d}_i \hat{\mathbf{d}}_3 + \dot{\mathbf{t}} + \boldsymbol{\omega} \times {}^B \mathbf{p}_i\right) = \frac{1}{2} \left(\dot{d}_i \hat{\mathbf{d}}_3 + \mathbf{J}_{pi,q} \dot{\mathbf{q}}\right) \tag{23}$$

Pre-multiplying both sides of Eq. (22) with $\hat{\mathbf{s}}_3^i$ yields:

$$\dot{d}_i = \hat{\mathbf{s}}_3^{iT} \dot{\mathbf{t}} + \left[\left({}^B \mathbf{R} \cdot {}^P \mathbf{p}_i \right) \times \hat{\mathbf{s}}_3^i \right]^T \boldsymbol{\omega} = \mathbf{J}_{d_i, q} \cdot \dot{\mathbf{q}} \quad (24)$$

$$\dot{\mathbf{D}} = \mathbf{J}_{d, q} \cdot \dot{\mathbf{q}} \quad (25)$$

where $\dot{\mathbf{D}} = [\dot{d}_1, \dot{d}_2, \dot{d}_3, \dot{d}_4, \dot{d}_5, \dot{d}_6]^T$ and $\mathbf{J}_{d, q}$ denotes the Jacobian matrix relating the general velocity to the sliding velocity of the actuator, which is given by:

$$\mathbf{J}_{d, q} = \begin{bmatrix} \hat{\mathbf{s}}_3^{1T} / \left(\hat{\mathbf{s}}_3^{1T} \hat{\mathbf{d}}_3^1 \right), \left[\left({}^B \mathbf{R} \cdot {}^P \mathbf{p}_1 \right) \times \hat{\mathbf{s}}_3^1 \right]^T / \left(\hat{\mathbf{s}}_3^{1T} \hat{\mathbf{d}}_3^1 \right) \\ \hat{\mathbf{s}}_3^{2T} / \left(\hat{\mathbf{s}}_3^{2T} \hat{\mathbf{d}}_3^2 \right), \left[\left({}^B \mathbf{R} \cdot {}^P \mathbf{p}_2 \right) \times \hat{\mathbf{s}}_3^2 \right]^T / \left(\hat{\mathbf{s}}_3^{2T} \hat{\mathbf{d}}_3^2 \right) \\ \hat{\mathbf{s}}_3^{3T} / \left(\hat{\mathbf{s}}_3^{3T} \hat{\mathbf{d}}_3^3 \right), \left[\left({}^B \mathbf{R} \cdot {}^P \mathbf{p}_3 \right) \times \hat{\mathbf{s}}_3^3 \right]^T / \left(\hat{\mathbf{s}}_3^{3T} \hat{\mathbf{d}}_3^3 \right) \\ \hat{\mathbf{s}}_3^{4T} / \left(\hat{\mathbf{s}}_3^{4T} \hat{\mathbf{d}}_3^4 \right), \left[\left({}^B \mathbf{R} \cdot {}^P \mathbf{p}_4 \right) \times \hat{\mathbf{s}}_3^4 \right]^T / \left(\hat{\mathbf{s}}_3^{4T} \hat{\mathbf{d}}_3^4 \right) \\ \hat{\mathbf{s}}_3^{5T} / \left(\hat{\mathbf{s}}_3^{5T} \hat{\mathbf{d}}_3^5 \right), \left[\left({}^B \mathbf{R} \cdot {}^P \mathbf{p}_5 \right) \times \hat{\mathbf{s}}_3^5 \right]^T / \left(\hat{\mathbf{s}}_3^{5T} \hat{\mathbf{d}}_3^5 \right) \\ \hat{\mathbf{s}}_3^{6T} / \left(\hat{\mathbf{s}}_3^{6T} \hat{\mathbf{d}}_3^6 \right), \left[\left({}^B \mathbf{R} \cdot {}^P \mathbf{p}_6 \right) \times \hat{\mathbf{s}}_3^6 \right]^T / \left(\hat{\mathbf{s}}_3^{6T} \hat{\mathbf{d}}_3^6 \right) \end{bmatrix} \quad (26)$$

Taking the derivative of both sides of Eq. (20) with respect to time, the acceleration of the actuator can be described by:

$$\mathbf{a}_{d_i}^c = \ddot{d}_i \hat{\mathbf{d}}_3^i \quad (27)$$

The same procedure can be easily adapted to obtain the acceleration of the centroid of the rod, which is given by:

$$\mathbf{a}_{s_i}^c = \frac{1}{2} \left[\ddot{d}_i \hat{\mathbf{d}}_3^i + \ddot{\mathbf{t}} + \boldsymbol{\omega} \times {}^B \mathbf{p}_i + \boldsymbol{\omega} \times \left(\boldsymbol{\omega} \times {}^B \mathbf{p}_i \right) \right] = \frac{1}{2} \left(\ddot{d}_i \hat{\mathbf{d}}_3^i + \mathbf{a}_{p_i} \right) \quad (28)$$

3.2. Partial velocity and partial angular velocity

To simplify the derivation, the base coordinate system can be represented by three unit vectors $\hat{\mathbf{i}} = [1, 0, 0]^T$, $\hat{\mathbf{j}} = [0, 1, 0]^T$ and $\hat{\mathbf{k}} = [0, 0, 1]^T$. The velocity of the center of mass and the angular velocity of the upper platform can also be described by:

$$\mathbf{v}_c = \dot{q}_1 \hat{\mathbf{i}} + \dot{q}_2 \hat{\mathbf{j}} + \dot{q}_3 \hat{\mathbf{k}} + \dot{q}_4 \hat{\mathbf{i}} \times \left({}^B \mathbf{R} \cdot {}^P \boldsymbol{\rho}_c \right) + \dot{q}_5 \hat{\mathbf{j}} \times \left({}^B \mathbf{R} \cdot {}^P \boldsymbol{\rho}_c \right) + \dot{q}_6 \hat{\mathbf{k}} \times \left({}^B \mathbf{R} \cdot {}^P \boldsymbol{\rho}_c \right) \quad (29)$$

$$\boldsymbol{\omega}_c = \dot{q}_4 \hat{\mathbf{i}} + \dot{q}_5 \hat{\mathbf{j}} + \dot{q}_6 \hat{\mathbf{k}} \quad (30)$$

where $\dot{q}_j (j = 1, \dots, 6)$ is the general velocity of the upper platform.

Therefore, the partial velocities and partial angular velocity of the upper platform can be obtained by inspection of the relevant velocity vectors:

$$\begin{aligned} \mathbf{v}_{c, q1} &= \hat{\mathbf{i}}, \mathbf{v}_{c, q2} = \hat{\mathbf{j}}, \mathbf{v}_{c, q3} = \hat{\mathbf{k}} \\ \mathbf{v}_{c, q4} &= \hat{\mathbf{i}} \times \left({}^B \mathbf{R} \cdot {}^P \boldsymbol{\rho}_c \right), \mathbf{v}_{c, q5} = \hat{\mathbf{j}} \times \left({}^B \mathbf{R} \cdot {}^P \boldsymbol{\rho}_c \right), \mathbf{v}_{c, q6} = \hat{\mathbf{k}} \times \left({}^B \mathbf{R} \cdot {}^P \boldsymbol{\rho}_c \right) \end{aligned} \quad (31)$$

$$\begin{aligned} \boldsymbol{\omega}_{c, q3} &= \boldsymbol{\omega}_{c, q2} = \boldsymbol{\omega}_{c, q1} = \mathbf{0} \\ \boldsymbol{\omega}_{c, q4} &= \hat{\mathbf{i}}, \boldsymbol{\omega}_{c, q5} = \hat{\mathbf{j}}, \boldsymbol{\omega}_{c, q6} = \hat{\mathbf{k}} \end{aligned} \quad (32)$$

Similarly, the partial velocities and partial angular velocities of the i^{th} rod can also be obtained:

$$\begin{aligned} \mathbf{v}_{s_i, q1}^c &= \frac{1}{2} \left(\mathbf{J}_{d, q}^{i,1} \cdot \hat{\mathbf{d}}_3^i + \hat{\mathbf{i}} \right), \mathbf{v}_{s_i, q2}^c = \frac{1}{2} \left(\mathbf{J}_{d, q}^{i,2} \cdot \hat{\mathbf{d}}_3^i + \hat{\mathbf{j}} \right), \mathbf{v}_{s_i, q3}^c = \frac{1}{2} \left(\mathbf{J}_{d, q}^{i,3} \cdot \hat{\mathbf{d}}_3^i + \hat{\mathbf{k}} \right) \\ \mathbf{v}_{s_i, q4}^c &= \frac{1}{2} \left(\mathbf{J}_{d, q}^{i,4} \cdot \hat{\mathbf{d}}_3^i + \hat{\mathbf{i}} \times {}^B \mathbf{p}_i \right), \mathbf{v}_{s_i, q5}^c = \frac{1}{2} \left(\mathbf{J}_{d, q}^{i,5} \cdot \hat{\mathbf{d}}_3^i + \hat{\mathbf{j}} \times {}^B \mathbf{p}_i \right), \mathbf{v}_{s_i, q6}^c = \frac{1}{2} \left(\mathbf{J}_{d, q}^{i,6} \cdot \hat{\mathbf{d}}_3^i + \hat{\mathbf{k}} \times {}^B \mathbf{p}_i \right) \end{aligned} \quad (33)$$

$$\begin{aligned}
 \omega_{si,q1}^c &= \hat{s}_3 \times (\hat{i} - J_{d,q}^{i,1} \cdot \hat{d}_3^i) / S_i, \quad \omega_{si,q2}^c = \hat{s}_3 \times (\hat{j} - J_{d,q}^{i,2} \cdot \hat{d}_3^i) / S_i, \quad \omega_{si,q3}^c = \hat{s}_3 \times (\hat{k} - J_{d,q}^{i,3} \cdot \hat{d}_3^i) / S_i \\
 \omega_{si,q4}^c &= \hat{s}_3 \times (\hat{i} \times {}^B p_i - J_{d,q}^{i,4} \cdot \hat{d}_3^i) / S_i, \quad \omega_{si,q5}^c = \hat{s}_3 \times (\hat{j} \times {}^B p_i - J_{d,q}^{i,5} \cdot \hat{d}_3^i) / S_i \\
 \omega_{si,q6}^c &= \hat{s}_3 \times (\hat{k} \times {}^B p_i - J_{d,q}^{i,6} \cdot \hat{d}_3^i) / S_i
 \end{aligned} \tag{34}$$

where $J_{d,q}^{ij}$ denotes the element on the i^{th} row and j^{th} column of Jacobian matrix $J_{d,q}$.

The partial velocities of the i^{th} actuator are given by:

$$\begin{aligned}
 v_{di,q1}^c &= J_{d,q}^{i,1} \cdot \hat{d}_3^i, \quad v_{di,q2}^c = J_{d,q}^{i,2} \cdot \hat{d}_3^i, \quad v_{di,q3}^c = J_{d,q}^{i,3} \cdot \hat{d}_3^i \\
 v_{di,q4}^c &= J_{d,q}^{i,4} \cdot \hat{d}_3^i, \quad v_{di,q5}^c = J_{d,q}^{i,5} \cdot \hat{d}_3^i, \quad v_{di,q6}^c = J_{d,q}^{i,6} \cdot \hat{d}_3^i
 \end{aligned} \tag{35}$$

The partial angular velocities of the i^{th} rod relating to the upper platform can be described by:

$$\omega_{pi,qj} = \omega_{c,qj} - \omega_{si,qj}^c \tag{36}$$

3.3. Rotational angle of the flexure joint

The lower flexure joint can be considered to be equivalent to a Hooke joint with torsional stiffness along its rotational axes, and the upper flexure joint can be considered to be equivalent to a 3-DOF universal joint with torsional stiffness along its rotational axes. Assuming that each rotation of the flexure joint occurs about an axis at a location dependent upon the preceding rotations, the rotation angles of the i^{th} upper flexure joints about the \hat{d}_1^i and the displaced two-axis are denoted by Q_1^{si} and Q_2^{si} , respectively.

The vector \mathbf{l}_{BP}^i can also be described by:

$$\mathbf{l}_{BP}^i = d_i \mathbf{d}_3^i + {}^B_{\hat{d}_i} \mathbf{R} \cdot \hat{s}_i \mathbf{R} \cdot \hat{s}_i \mathbf{p}_i \tag{37}$$

where ${}^B_{\hat{d}_i} \mathbf{R}$ is the rotation matrix of the transformation from the reference frame \hat{d}_i to the base frame $\{B\}$, ${}^{\hat{d}_i}_{\hat{s}_i} \mathbf{R}$ is the rotation matrix of the translation from the reference frame \hat{s}_i to the reference frame \hat{d}_i , which adopts Z-Y-X Euler angles, $\hat{s}_i \mathbf{p}_i$ is the position vector of point P_i under frame $\hat{s}_i \mathbf{p}_i$.

Using Eq. (37), the following expression can be obtained:

$${}^{\hat{d}_i}_{\hat{s}_i} \mathbf{R} \cdot \hat{s}_i \mathbf{p}_i = {}^B_{\hat{d}_i} \mathbf{R}^T (\mathbf{l}_{BP}^i - d_i \mathbf{d}_3^i) \tag{38}$$

Let ${}^B_{\hat{d}_i} \mathbf{R}^T (\mathbf{l}_{BP}^i - d_i \mathbf{d}_3^i) = \mathbf{A}$, then Eq. (38) can be rewritten as:

$$\begin{bmatrix} \cos Q_2^{si} & 0 & \sin Q_2^{si} \\ \sin Q_1^{si} \sin Q_2^{si} & \cos Q_1^{si} & -\sin Q_1^{si} \cos Q_2^{si} \\ -\cos Q_1^{si} \sin Q_2^{si} & \sin Q_1^{si} & \cos Q_1^{si} \cos Q_2^{si} \end{bmatrix} \begin{bmatrix} 0 \\ 0 \\ S_i \end{bmatrix} = \mathbf{A} \tag{39}$$

Simplifying Eq. (39) yields:

$$\begin{bmatrix} \sin Q_2^{si} \cdot S_i \\ -\sin Q_1^{si} \cos Q_2^{si} \cdot S_i \\ \cos Q_1^{si} \cos Q_2^{si} \cdot S_i \end{bmatrix} = \mathbf{A} \tag{40}$$

Using Eq. (40), the rotation angles Q_1^{si} and Q_2^{si} can be obtained:

$$Q_1^{si} = -\arctan\left(\frac{A_2}{A_3}\right), \quad Q_2^{si} = \arcsin\left(\frac{A_1}{S_i}\right) \tag{41}$$

where A_i is the i^{th} element of the vector \mathbf{A} .

The rotation matrix can be described by:

$${}^B \mathbf{R} = {}^B_{\hat{d}_i} \mathbf{R} \cdot {}^{\hat{d}_i}_{\hat{s}_i} \mathbf{R} \cdot \hat{s}_i \mathbf{R} \cdot \hat{s}_i^* \mathbf{R} \tag{42}$$

where $\hat{\mathbf{S}}_i^* \mathbf{R}$ is the rotation matrix of the transformation from the reference frame $\hat{\mathbf{S}}_i^*$ to frame $\hat{\mathbf{S}}_i$ and $\hat{\mathbf{S}}_i^* \mathbf{R}$ is the rotation matrix of the transformation from the body frame {P} to frame $\hat{\mathbf{S}}_i^*$.

Using Eq. (42), the rotation matrix $\hat{\mathbf{S}}_i^* \mathbf{R}$ can be written as:

$$\hat{\mathbf{S}}_i^* \mathbf{R} = \hat{\mathbf{d}}_i \mathbf{R}^T \cdot \hat{\mathbf{B}} \mathbf{R}^T \cdot \hat{\mathbf{B}}_P \mathbf{R} \cdot \hat{\mathbf{s}}_i^* \mathbf{R}^T \tag{43}$$

$$\hat{\mathbf{S}}_i^* \mathbf{R} = \begin{bmatrix} c_2^{pi} c_3^{pi} & -c_2^{pi} s_3^{pi} & s_2^{pi} \\ s_1^{pi} s_2^{pi} c_3^{pi} + c_1^{pi} s_3^{pi} & -s_1^{pi} s_2^{pi} s_3^{pi} + c_1^{pi} c_3^{pi} & -s_1^{pi} c_2^{pi} \\ -c_1^{pi} s_2^{pi} c_3^{pi} + s_1^{pi} s_3^{pi} & c_1^{pi} s_2^{pi} s_3^{pi} + s_1^{pi} c_3^{pi} & c_1^{pi} c_2^{pi} \end{bmatrix} \tag{44}$$

where c_k^{pi} and s_k^{pi} represent the cosine and sine of the respective rotation angles Q_k^{pi} ($k = 1, 2, 3$) of the upper flexure joints.

Let $\hat{\mathbf{d}}_i \mathbf{R}^T \cdot \hat{\mathbf{B}} \mathbf{R}^T \cdot \hat{\mathbf{B}}_P \mathbf{R} \cdot \hat{\mathbf{s}}_i^* \mathbf{R}^T = \mathbf{B}$, and substituting this into Eq. (44), the rotation angles Q_1^{pi} , Q_2^{pi} and Q_3^{pi} can be obtained as:

$$Q_1^{pi} = -\arctan(B_{2,3}/B_{3,3}), Q_2^{pi} = \arcsin(B_{1,3}), Q_3^{pi} = -\arctan(B_{1,2}/B_{1,1}) \tag{45}$$

where $B_{i,j}$ represents an element on the i^{th} row and j^{th} column of matrix \mathbf{B} .

3.4. Dynamic equations

For the j^{th} generalized speed, the upper platforms contribution to the set of generalized active forces is:

$$\mathbf{Q}_{P,qj} = \mathbf{v}_{c,qj} (m_P \mathbf{g} + \mathbf{F}_D) + \boldsymbol{\omega}_{c,qj} \mathbf{M}_D \tag{46}$$

where \mathbf{F}_D and \mathbf{M}_D are the external force and the moment acting on the original point of the body frame, respectively.

Let \mathbf{M}_1^i and \mathbf{M}_2^i represent the elastic moments of the lower flexure joint and upper flexure joint, respectively, which are given by:

$$\mathbf{M}_1^i = k_1^i Q_1^{si} \hat{\mathbf{c}}_1^{si} + k_2^i Q_2^{si} \hat{\mathbf{m}}_2^{si} \tag{47}$$

$$\mathbf{M}_2^i = k_1^i Q_1^{pi} \hat{\mathbf{c}}_1^{pi} + k_2^i Q_2^{pi} \hat{\mathbf{m}}_2^{pi} + k_3^i Q_3^{pi} \hat{\mathbf{n}}_3^{pi} \tag{48}$$

where k_1^i and k_2^i are the torsional stiffness coefficients of the i^{th} lower flexure joint about the axis $\hat{\mathbf{c}}_1^{si}$ ($\hat{\mathbf{c}}_1^{si} = \hat{\mathbf{d}}_1^i$) and the moved two-axis $\hat{\mathbf{m}}_2^{si}$, respectively; and k_1^i , k_2^i and k_3^i are the torsional stiffness coefficients of the i^{th} upper flexure joint about the axis $\hat{\mathbf{c}}_1^{pi}$ ($\hat{\mathbf{c}}_1^{pi} = \hat{\mathbf{s}}_1^i$), the moved two-axis $\hat{\mathbf{m}}_2^{pi}$ and the moved three-axis $\hat{\mathbf{n}}_3^{pi}$, respectively.

The axes $\hat{\mathbf{m}}_2^{si}$, $\hat{\mathbf{m}}_2^{pi}$ and $\hat{\mathbf{n}}_3^{pi}$ are given by:

$$\hat{\mathbf{m}}_2^{si} = \begin{bmatrix} 1 & 0 & 0 \\ 0 & \cos Q_1^{si} & -\sin Q_1^{si} \\ 0 & \sin Q_1^{si} & \cos Q_1^{si} \end{bmatrix} \hat{\mathbf{d}}_2^i \tag{49}$$

$$\hat{\mathbf{m}}_2^{pi} = \begin{bmatrix} 1 & 0 & 0 \\ 0 & \cos Q_1^{pi} & -\sin Q_1^{pi} \\ 0 & \sin Q_1^{pi} & \cos Q_1^{pi} \end{bmatrix} \hat{\mathbf{s}}_2^i \tag{50}$$

$$\hat{\mathbf{n}}_3^{pi} = \begin{bmatrix} \cos Q_2^{pi} & 0 & \sin Q_2^{pi} \\ \sin Q_1^{pi} \sin Q_2^{pi} & \cos Q_1^{pi} & -\sin Q_1^{pi} \cos Q_2^{pi} \\ -\cos Q_1^{pi} \sin Q_2^{pi} & \sin Q_1^{pi} & \cos Q_1^{pi} \cos Q_2^{pi} \end{bmatrix} \hat{\mathbf{s}}_3^i \tag{51}$$

The contribution of each rod to the set of generalized speeds is:

$$\mathbf{Q}_{si,qj}^c = \mathbf{v}_{si,qj}^c m_{si} \mathbf{g} - (\boldsymbol{\omega}_{si,qj}^c \mathbf{M}_1^i + \boldsymbol{\omega}_{pi,qj} \mathbf{M}_2^i) \tag{52}$$

Let F_{di} represent the force exerted by the i^{th} actuator and k_e^i represent the stiffness of the membranes of the i^{th} actuator. The contribution of each actuator to the set of generalized speeds can be derived by:

$$\mathbf{Q}_{di,qj}^c = \mathbf{v}_{di,qj}^c (m_{di} \mathbf{g} + F_{di} \hat{\mathbf{d}}_3^i - k_e^i \Delta d_i \hat{\mathbf{d}}_3^i) \tag{53}$$

The contributions of the upper platform, rods and actuators to the generalized inertial forces for the i^{th} generalized speed are:

$$\mathbf{Q}_{p,qj}^* = \mathbf{v}_{c,qj} (-m_p \mathbf{a}_c) + \omega_{c,qj} \left[-{}^B \mathbf{I}_c \dot{\boldsymbol{\omega}} - \boldsymbol{\omega} \times ({}^B \mathbf{I}_c \boldsymbol{\omega}) \right] \quad (54)$$

$$\mathbf{Q}_{si,qj}^{c*} = \mathbf{v}_{si,qj}^c (-m_{si} \mathbf{a}_{si}^c) + \omega_{si,qj}^c \left[-{}^B \mathbf{I}_{si}^c \dot{\boldsymbol{\omega}}_{si} - \boldsymbol{\omega}_{si} \times ({}^B \mathbf{I}_{si}^c \boldsymbol{\omega}_{si}) \right] \quad (55)$$

$$\mathbf{Q}_{di,qj}^{c*} = \mathbf{v}_{di,qj}^c (-m_{si} \mathbf{a}_{di}^c) \quad (56)$$

where ${}^P \mathbf{I}_c$ is the inertia matrix of the upper platform with respect to its center of mass in the body frame, ${}^B \mathbf{I}_c = {}^B \mathbf{R} \cdot {}^P \mathbf{I}_c \cdot {}^B \mathbf{R}^T$ and is the inertia matrix of the i^{th} rod with respect to its center of mass in the base frame.

The holonomic generalized active for the j^{th} ($j = 1, \dots, 6$) generalized speed is:

$$\mathbf{F}_{qj} = \mathbf{Q}_{p,qj} + \sum_{i=1}^6 \mathbf{Q}_{si,qj}^c + \sum_{i=1}^6 \mathbf{Q}_{di,qj}^c \quad (57)$$

Likewise, the contribution to the set of holonomic generalized inertia force is:

$$\mathbf{F}_{qj}^* = \mathbf{Q}_{p,qj}^* + \sum_{i=1}^6 \mathbf{Q}_{si,qj}^{c*} + \sum_{i=1}^6 \mathbf{Q}_{di,qj}^{c*} \quad (58)$$

Kane's dynamic equations are:

$$\mathbf{F}_{qj} + \mathbf{F}_{qj}^* = \mathbf{0} \quad (j = 1, \dots, 6) \quad (59)$$

The effect of gravity on the moving platform and the actuators can be compensated for by the elastic forces of the membrane of the actuators, i.e. the moving platform will move to a new equilibrium position. Therefore, the effect of gravity on the micro-vibration simulator can be ignored. The final expression of Eq. (59) can be written as:

$$m_p \mathbf{v}_{c,qj} \mathbf{a}_c + \omega_{c,qj} \left[{}^B \mathbf{I}_c \dot{\boldsymbol{\omega}} + \boldsymbol{\omega} \times ({}^B \mathbf{I}_c \boldsymbol{\omega}) \right] + \sum_{i=1}^6 \left\{ m_{si} \mathbf{v}_{si,qj}^c \mathbf{a}_{si}^c + \omega_{si,qj}^c \left[{}^B \mathbf{I}_{si}^c \dot{\boldsymbol{\omega}}_{si} + \boldsymbol{\omega}_{si} \times ({}^B \mathbf{I}_{si}^c \boldsymbol{\omega}_{si}) \right] \right. \\ \left. + \left(\omega_{si,qj}^c \mathbf{M}_1^i + \omega_{pi,qj} \mathbf{M}_2^i \right) + \mathbf{v}_{di,qj}^c \left(m_{si} \mathbf{a}_{di}^c + k_e^i \Delta d_i \hat{\mathbf{d}}_3^i \right) \right\} = \sum_{i=1}^6 \mathbf{v}_{di,qj}^c \left(F_{di} \hat{\mathbf{d}}_3^i \right) \quad (j = 1, \dots, 6) \quad (60)$$

The complete dynamic equation of the 6-DOF micro-vibration simulator can be derived by:

$$\mathbf{M}(\mathbf{q}) \ddot{\mathbf{q}} + \mathbf{C}(\mathbf{q}, \dot{\mathbf{q}}) \dot{\mathbf{q}} + \mathbf{K}(\mathbf{q}) \mathbf{q} = \mathbf{J}_{d,q}^T \mathbf{F}_d \quad (61)$$

where $\mathbf{M}(\mathbf{q})$ is a 6×6 mass matrix, $\mathbf{C}(\mathbf{q}, \dot{\mathbf{q}})$ is a 6×6 matrix of the centrifugal and Coriolis force terms, $\mathbf{K}(\mathbf{q})$ is a 6×6 matrix of the generalized stiffness and \mathbf{F}_d is a 6×1 vector representing the excitation forces.

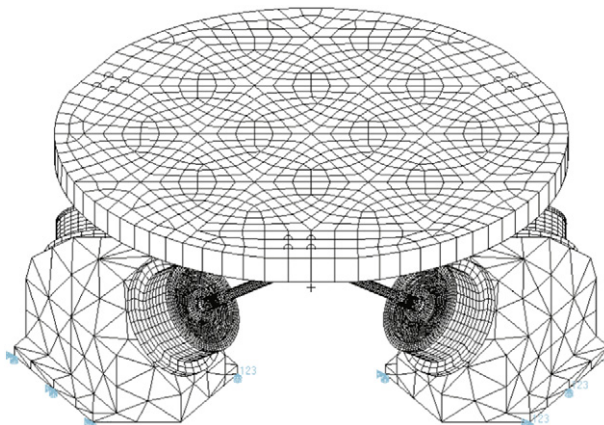


Fig. 5. The finite element model of the 6-MVS.

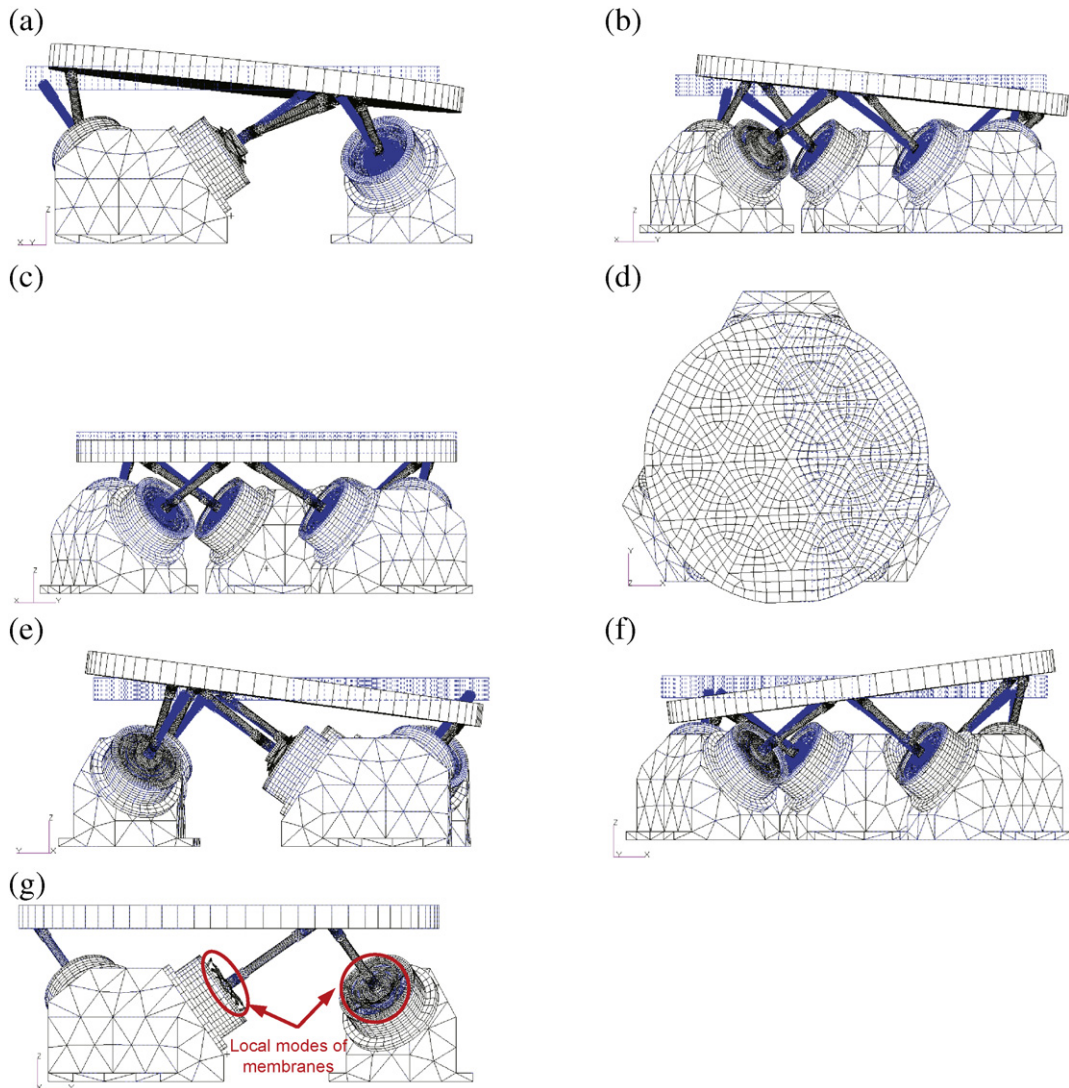


Fig. 6. Mode shapes of the first seven modes of the finite element model of the 6-MVS: (a) tilting mode along y-axis at 9.06Hz, (b) tilting mode along x-axis at 9.06Hz, (c) piston mode along z-axis at 10.2Hz, (d) twisting around z-axis at 12.88Hz, (e) rolling mode around x-axis at 13.69Hz, (f) rolling mode around y-axis at 13.69Hz, (g) local mode of membrane at 526.9Hz.

4. Finite element analysis

In this paper, the dynamic model of the mechanical system for the parallel robot is viewed as thirteen rigid bodies. However, when there are high-frequency exciting forces acting on an actual system, elastic deformations need to be taken into account. The results of mode analysis characterize the basic dynamic behavior of the structure and are an indication of how the structure will respond to dynamic loading. Therefore, the finite element method is adopted to analyze the normal mode of the 6-MVS. A finite element model of the 6-MVS was developed by MSC NASTRAN software, and is depicted in Fig. 5. The upper platform is modeled using a combination of Hex8, Wedge 6, Tria3 and Quad4 elements. The membranes are modeled using Quad4 elements, and the other components are modeled using CTETRA elements or other solid elements. All bolted connections between different components are simulated by node coupling.

From Fig. 6, it can be seen that the natural frequency of the bending mode of the membrane is above 500 Hz. There is no resonance peak between 0 Hz and 9 Hz, which is attributed to the simulator reproducing low frequency micro-vibrations. Although six resonance peaks exist between 9 and 14 Hz, they are all body modes due to the elastic elements including the membranes and the flexure joints, rather than flexible body modes (bending modes). Furthermore, these resonance peaks can be offset by force compensation. There is no flexible body mode between 14 and 520 Hz. Therefore, within this frequency range,

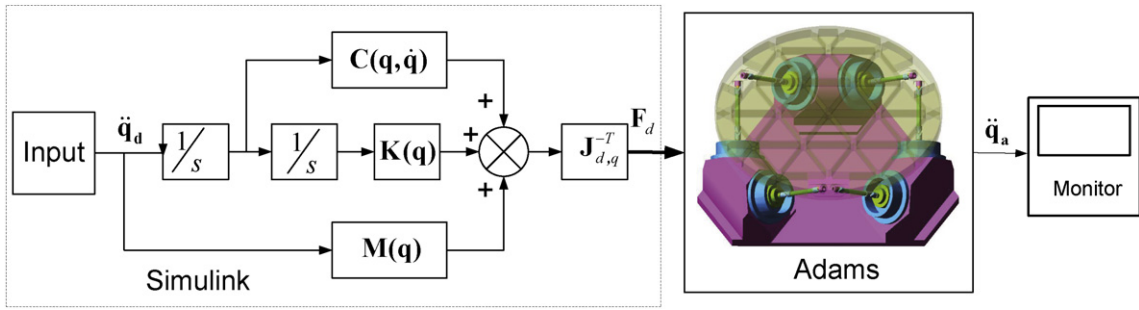


Fig. 7. Co-simulation block diagram.

the 6-MVS has excellent dynamic performance, which is a benefit to the simulator for reproduction of high frequency micro-vibrations. It can be concluded that the structural performance of the 6-MVS satisfies the structural demands of the regeneration of the micro-vibration spectrum with a width bandwidth of disturbance frequencies.

5. Dynamic model verification

The main objective of the proposed inverse dynamic model is to compute the required actuator forces when given the desired accelerations at different frequencies. However, the accuracy and effectiveness of the developed dynamic model have not yet been verified. In this section, a co-simulation using ADAMS and MATLAB/Simulink has been adopted to verify the validity of the dynamic model and the feasibility of the 6-MVS. The MATLAB/Simulink environment is used to compute the required actuator forces and ADAMS is used to build the virtual prototype of the 6-MVS. The six excitation forces of the actuators are used as inputs to derive the ADAMS model and the accelerations and angular accelerations of the upper platform are used as the outputs of the ADAMS plant model. Fig. 7 shows the ADAMS model and the co-simulation block diagram.

In ADAMS, the structural parameters and mass properties of the 6-MVS are shown in Tables 1 and 2, respectively. The upper platform is allowed to track three translational acceleration trajectories and three angular acceleration trajectories at the same time, i.e.

$$\begin{aligned} \ddot{q}_{d1} &= 0.004 \cos(4\pi \cdot t) + 0.004 \cos(10\pi \cdot t) \\ \ddot{q}_{d2} &= 0.001 \cos(4\pi \cdot t) + 0.002 \cos(10\pi \cdot t) \\ \ddot{q}_{d3} &= 0.005 \cos(4\pi \cdot t) + 0.0015 \cos(10\pi \cdot t) \\ \ddot{q}_{d4} &= 0.02 \cos(4\pi \cdot t) + 0.012 \cos(10\pi \cdot t) \\ \ddot{q}_{d5} &= 0.01 \cos(4\pi \cdot t) + 0.014 \cos(10\pi \cdot t) \\ \ddot{q}_{d6} &= 0.01 \cos(4\pi \cdot t) + 0.02 \cos(10\pi \cdot t) \end{aligned}$$

where t is the time variable in unit seconds, \ddot{q}_{d1} , \ddot{q}_{d2} and \ddot{q}_{d3} are in units of meters per second squared, and \ddot{q}_{d4} , \ddot{q}_{d5} and \ddot{q}_{d6} are in units of radians per second squared.

Fig. 8 compares the desired and simulated accelerations of the upper platform. The desired acceleration curves are the input acceleration trajectories, and the simulated acceleration curves are the output acceleration trajectories of the ADAMS model. Fig. 8 shows clear consistency between the translational accelerations and angular accelerations produced by the 6-MVS and the target acceleration trajectories.

Table 1
Structural parameters of the 6-DOF micro-vibration simulator.

Notation	Specification	Value
R_p	Upper platform radius	220 mm
R_B	Base plane radius	230 mm
H	Height of the origin of the body frame in the base frame	146 mm
φ	Upper platform central angle	10.8°
θ	Base plane central angle	120°
s_i	Length of the rod	100 mm
d_0	Initial length of the actuator	152.68 mm
z_{cm}	Height of the centroid of the moving platform in the body frame	1.72 mm
k	Axial stiffness of membrane	$2.16 \times 10^4 \text{ N m}^{-1}$
k_θ	Torsional stiffness coefficients of the flexure joint	48.67 N m/rad

Table 2

Mass properties of the 6-DOF micro-vibration simulator.

Notation	Specification	Value
m	Mass of the upper platform	19 kg
I_{xx}	Moment of inertia of the upper platform about x-axis	0.3314 kg m ²
I_{yy}	Moment of inertia of the upper platform about y-axis	0.3125 kg m ²
I_{zz}	Moment of inertia of the upper platform about z-axis	0.6571 kg m ²
m_{si}	Mass of the rod	0.068 kg
m_{di}	Mass of actuator	0.206 kg
I_{siox}	Moment of inertia of the rod about the x-axis	6.1×10^{-5} kg m ²
I_{siyy}	Moment of inertia of the rod about the y-axis	6.1×10^{-5} kg m ²
I_{sizz}	Moment of inertia of the rod about the z-axis	1.1×10^{-5} kg m ²

6. Control strategy and simulation

The model implemented in Section 5 is an ideal model. However, since an actual 6-MVS will not exactly coincide with the theoretical model, a control measure needs to be implemented for the 6-MVS. The classical computed torque control (CTC) approach uses an inverse dynamic model to decouple and linearize the nonlinear dynamics of the parallel manipulator. Therefore, if the dynamic model is accurate enough, the resulting system will be a series of decoupled linear systems that can be easily controlled using a proportional-derivative (PD) based control law.

6.1. Computed torque control

Dynamics control in task space utilizing the CTC method is implemented for the 6-MVS as follows. Firstly, the task space dynamic model in Eq. (61) can be rewritten into the form:

$$\mathbf{F}_q = \mathbf{J}_{d,q}^T \mathbf{F}_d = \mathbf{M}(\mathbf{q}) \ddot{\mathbf{q}} + \mathbf{H}(\mathbf{q}, \dot{\mathbf{q}}) \quad (62)$$

where $\mathbf{H}(\mathbf{q}, \dot{\mathbf{q}}) = \mathbf{C}(\mathbf{q}, \dot{\mathbf{q}}) \dot{\mathbf{q}} + \mathbf{K}(\mathbf{q}) \mathbf{q}$.

The block diagram of the CTC scheme with PD feedback is depicted in Fig. 9. The 6-MVS is actuated by the following actuator forces described in the task space, assuming no external disturbances:

$$\mathbf{F}_q = \mathbf{M}(\mathbf{q}) \mathbf{u} + \mathbf{H}(\mathbf{q}, \dot{\mathbf{q}}) \quad (63)$$

where \mathbf{u} is an input signal vector in the form of acceleration.

Combining Eq. (62) with Eq. (63) results in the following linear second-order system

$$\ddot{\mathbf{q}} = \mathbf{u} \quad (64)$$

which indicates that the system of Eq. (63) under control in Eq. (64) is linear and decoupled with respect to the input vector \mathbf{u} .

The acceleration input signal in Eq. (63) can be described by:

$$\mathbf{u} = \mathbf{q}_d + \mathbf{K}_D(\dot{\mathbf{q}}_d - \dot{\mathbf{q}}) + \mathbf{K}_P(\mathbf{q}_d - \mathbf{q}) \quad (65)$$

Substituting Eq. (65) into Eq. (64) yields a homogeneous second-order differential equation of errors, which is given by:

$$\ddot{\mathbf{e}} + \mathbf{K}_D \dot{\mathbf{e}} + \mathbf{K}_P \mathbf{e} = \mathbf{0} \quad (66)$$

where $\mathbf{e} = \mathbf{q}_d - \mathbf{q}$ is the vector of the displacement tracking errors. It has been shown that the displacement and acceleration tracking errors in Eq. (66) are asymptotically stable along with the positive definite matrices \mathbf{K}_P and \mathbf{K}_D .

In real situations, the payload and dynamic parameters, including the stiffness coefficients of the flexure joints and membranes, may not be exactly known, despite the CTC scheme with PD feedback having excellent control performance. There can be a high degradation of control accuracy of the system due to this difference between an actual system and the ideal model. Thus the control performance is limited, which provides the motivation for the design of a robust controller in the following section.

6.2. CTC based robust PI control

Referring to the dynamic Eqs. (61) and (62), in the presence of uncertainties such as modeling errors, unknown loads, and parameter measurements, the 6-MVS is actuated with the following actuator forces expressed in the task space:

$$\mathbf{F}_q = \hat{\mathbf{M}}(\mathbf{q}) \ddot{\mathbf{q}} + \hat{\mathbf{C}}(\mathbf{q}, \dot{\mathbf{q}}) \dot{\mathbf{q}} + \hat{\mathbf{K}}(\mathbf{q}) \mathbf{q} \quad (67)$$

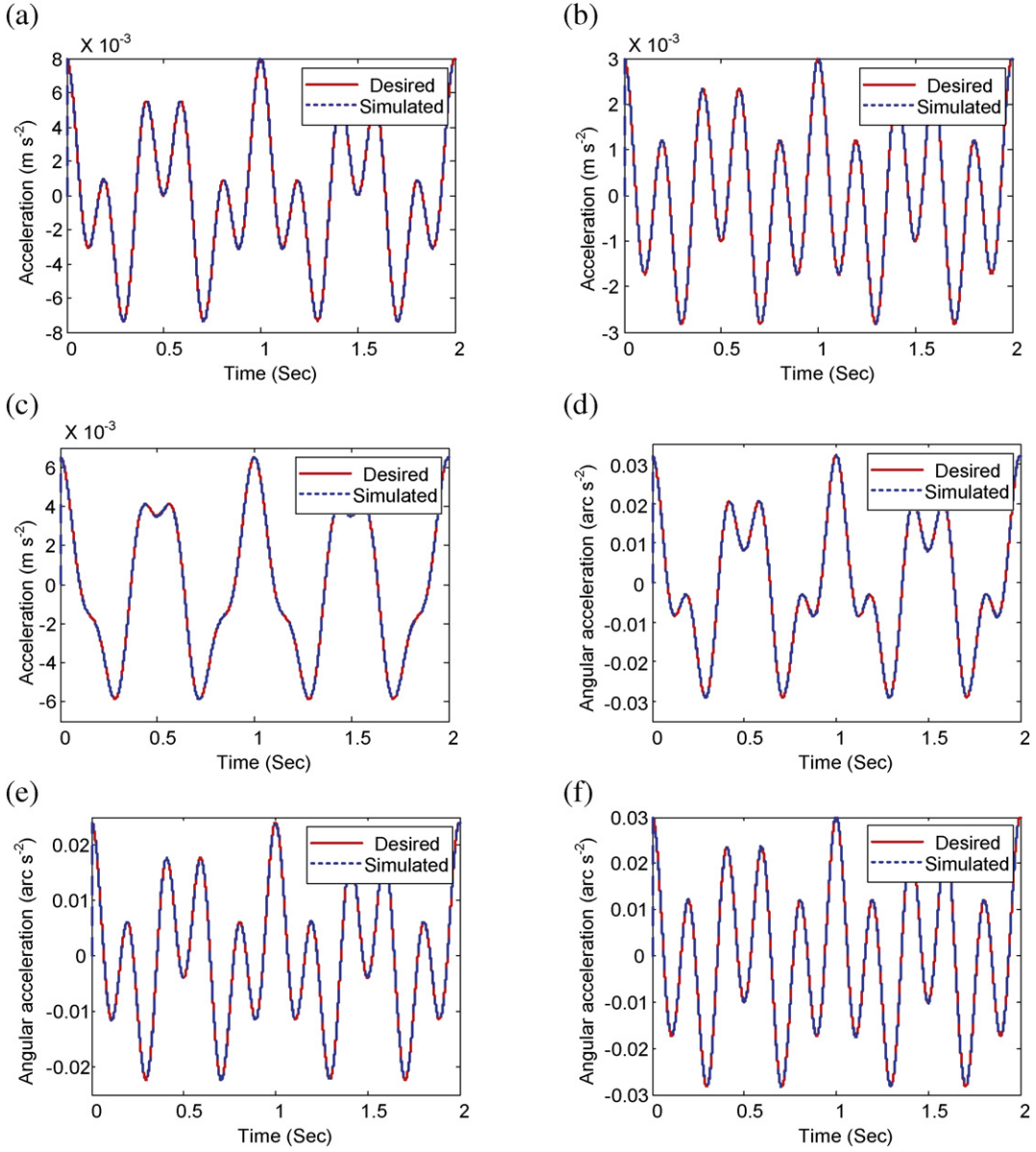


Fig. 8. Comparison of desired and simulated accelerations of the upper platform in the time domain: (a) translational accelerations along the x-axis, (b) translational accelerations along the y-axis, (c) translational accelerations along the z-axis, (d) angular accelerations about the x-axis, (e) angular accelerations about the y-axis, (f) angular accelerations about the z-axis.

where $\hat{M}(\mathbf{q})$, $\hat{C}(\mathbf{q}, \dot{\mathbf{q}})$ and $\hat{K}(\mathbf{q})$ denote the estimators of the mass matrix $M(\mathbf{q})$, the nonlinear coupling matrix $C(\mathbf{q}, \dot{\mathbf{q}})$ and the generalized stiffness $K(\mathbf{q})$ implemented in the controller, respectively. The errors of these estimates, i.e., the uncertainties, can be expressed by:

$$\mathbf{E}_M = \hat{M}(\mathbf{q}) - M(\mathbf{q}), \mathbf{E}_C = \hat{C}(\mathbf{q}, \dot{\mathbf{q}}) - C(\mathbf{q}, \dot{\mathbf{q}}), \mathbf{E}_K = \hat{K}(\mathbf{q}) - K(\mathbf{q}) \quad (68)$$

The error function is defined as:

$$\mathbf{r} = \dot{\mathbf{e}} + \Lambda \mathbf{e} \quad (69)$$

Let $\dot{\mathbf{q}}_r = \mathbf{r}(t) + \dot{\mathbf{q}}(t)$ and $\ddot{\mathbf{q}}_r = \dot{\mathbf{r}}(t) + \ddot{\mathbf{q}}(t)$, the following equation can be obtained:

$$\dot{\mathbf{q}}_r = \dot{\mathbf{q}}_d + \Lambda \mathbf{e}, \ddot{\mathbf{q}}_r = \ddot{\mathbf{q}}_d + \Lambda \dot{\mathbf{e}} \quad (70)$$

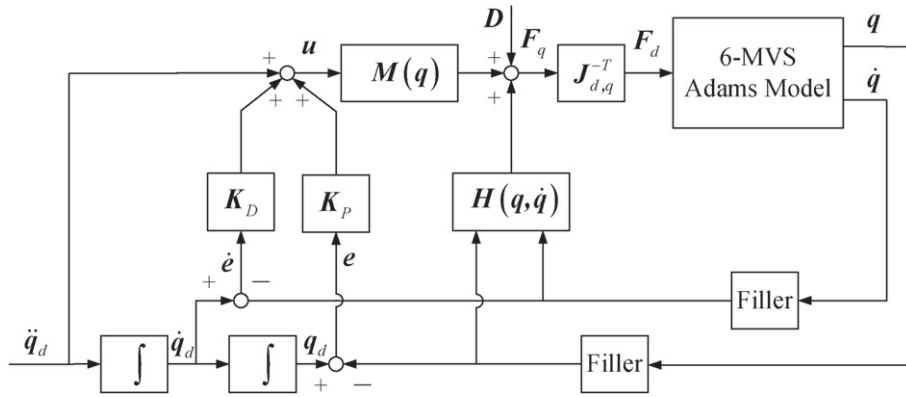


Fig. 9. Block diagram of proportional-derivative feedback control based on computed torque.

where Λ is a 6×6 diagonal constant matrix of positive gain.

Substituting Eqs. (70) and (68) into Eq. (67) yields:

$$\begin{aligned}
 \mathbf{F}_q &= \hat{\mathbf{M}}(\mathbf{q}) \ddot{\mathbf{q}} + \hat{\mathbf{C}}(\mathbf{q}, \dot{\mathbf{q}}) \dot{\mathbf{q}} + \hat{\mathbf{K}}(\mathbf{q}) \mathbf{q} \\
 &= \hat{\mathbf{M}}(\mathbf{q}) (\ddot{\mathbf{q}}_r - \ddot{\mathbf{r}}) + \hat{\mathbf{C}}(\mathbf{q}, \dot{\mathbf{q}}) (\dot{\mathbf{q}}_r - \dot{\mathbf{r}}) + \hat{\mathbf{K}}(\mathbf{q}) \mathbf{q} \\
 &= (\mathbf{M}(\mathbf{q}) + \mathbf{E}_M) \ddot{\mathbf{q}}_r + (\mathbf{C}(\mathbf{q}, \dot{\mathbf{q}}) + \mathbf{E}_C) \dot{\mathbf{q}}_r + (\mathbf{K}(\mathbf{q}) + \mathbf{E}_K) \mathbf{q} - \hat{\mathbf{M}}(\mathbf{q}) \ddot{\mathbf{r}} - \hat{\mathbf{C}}(\mathbf{q}, \dot{\mathbf{q}}) \dot{\mathbf{r}} \\
 &= \mathbf{M}(\mathbf{q}) \ddot{\mathbf{q}}_r + \mathbf{C}(\mathbf{q}, \dot{\mathbf{q}}) \dot{\mathbf{q}}_r + \mathbf{K}(\mathbf{q}) \mathbf{q} - \hat{\mathbf{M}}(\mathbf{q}) \ddot{\mathbf{r}} - \hat{\mathbf{C}}(\mathbf{q}, \dot{\mathbf{q}}) \dot{\mathbf{r}} + \mathbf{E}_{EOR}
 \end{aligned} \tag{71}$$

where $\mathbf{E}_{EOR} = \mathbf{E}_M \ddot{\mathbf{q}}_r + \mathbf{E}_C \dot{\mathbf{q}}_r + \mathbf{E}_K \mathbf{q}$.

The control law is designed as:

$$\mathbf{F}_q = \mathbf{F}_m + \mathbf{K}_p \mathbf{r} + \mathbf{K}_i \int_0^t \mathbf{r} dt + \boldsymbol{\tau}_r \tag{72}$$

where \mathbf{K}_p is a 6×6 proportional-gain positive definite matrix, $\mathbf{K}_p > 0$, \mathbf{K}_i is a 6×6 integral-time positive definite matrix, $\mathbf{K}_i > 0$, \mathbf{F}_m is the control term of the normal dynamic model, and $\boldsymbol{\tau}_r$ is the robustness term due to model errors and friction disturbance, given by:

$$\mathbf{F}_m = \mathbf{M}(\mathbf{q}) \ddot{\mathbf{q}}_r + \mathbf{C}(\mathbf{q}, \dot{\mathbf{q}}) \dot{\mathbf{q}}_r + \mathbf{K}(\mathbf{q}) \mathbf{q}, \boldsymbol{\tau}_r = \mathbf{K}_r \text{sgn}(\mathbf{r}) \tag{73}$$

where $\mathbf{K}_r = \text{diag}[k_{r_{ii}}], k_{r_{ii}} \geq |E_{EOR}^i|, i = 1, \dots, n$.

Combining Eq. (71) with Eq. (72) and simplifying yields:

$$\hat{\mathbf{M}}(\mathbf{q}) \ddot{\mathbf{r}} + \hat{\mathbf{C}}(\mathbf{q}, \dot{\mathbf{q}}) \dot{\mathbf{r}} + \mathbf{K}_i \int_0^t \mathbf{r} dt = -\mathbf{K}_p \mathbf{r} - \mathbf{K}_r \text{sgn}(\mathbf{r}) + \mathbf{E}_{EOR} \tag{74}$$

The Lyapunov function candidate for the system in Eq. (74) is defined as:

$$V = \frac{1}{2} \mathbf{r}^T \hat{\mathbf{M}}(\mathbf{q}) \mathbf{r} + \frac{1}{2} \left(\int_0^t \mathbf{r} d\tau \right)^T \mathbf{K}_i \left(\int_0^t \mathbf{r} d\tau \right) \tag{75}$$

Hence, the derivative of the Lyapunov candidate function becomes:

$$\dot{V} = \mathbf{r}^T \left[\hat{\mathbf{M}}(\mathbf{q}) \ddot{\mathbf{r}} + \frac{1}{2} \dot{\hat{\mathbf{M}}}(\mathbf{q}) \mathbf{r} + \mathbf{K}_i \left(\int_0^t \mathbf{r} d\tau \right) \right] \tag{76}$$

Table 3
Target frequency spectrum of translational and angular acceleration.

Frequency (Hz)	$A_x(\text{mm} \cdot \text{s}^{-2})$	$A_y(\text{mm} \cdot \text{s}^{-2})$	$A_z(\text{mm} \cdot \text{s}^{-2})$	$A_{rx}(\text{mm} \cdot \text{s}^{-2})$	$A_{ry}(\text{mm} \cdot \text{s}^{-2})$	$A_{rz}(\text{mm} \cdot \text{s}^{-2})$
10	2.0	1.0	1.5	0.02	0.01	0.01
50	1.2	1.3	1.1	0.015	0.014	0.013
100	1.1	1.2	1.0	0.01	0.012	0.014

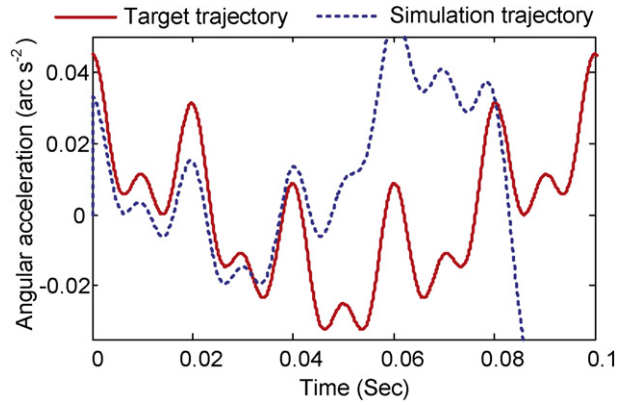


Fig. 10. Simulation result of robust PI controller.

The skew symmetric property of $\hat{M}(\mathbf{q}) - 2\hat{C}(\mathbf{q}, \dot{\mathbf{q}})$ given in Eq. (76) can then be rewritten as:

$$\dot{V} = \mathbf{r}^T \left[\hat{M}(\mathbf{q}) \dot{\mathbf{r}} + \hat{C}(\mathbf{q}, \dot{\mathbf{q}}) \mathbf{r} + \mathbf{K}_i \left(\int_0^t \mathbf{r} d\tau \right) \right] \quad (77)$$

Substituting Eq. (74) into Eq. (77) yields

$$\dot{V} = -\mathbf{r}^T \mathbf{K}_p \mathbf{r} + \mathbf{r}^T \mathbf{E}_{EOR} - \mathbf{r}^T \mathbf{K}_r \text{sgn}(\mathbf{r}) \quad (78)$$

Considering that the definition of $k_{r_{ii}} \geq |E_{EOR,i}|$, the following expression can be obtained:

$$\dot{V} \leq -\mathbf{r}^T \mathbf{K}_p \mathbf{r} \leq 0 \quad (79)$$

which indicates that the control system is practically stable.

6.3. Simulation results

In order to implement the control scheme presented above, several control parameters in terms of $\mathbf{K}_i, \mathbf{K}_p, \mathbf{\Lambda}, \mathbf{K}_r$, have to be determined. Generally, the greater the uncertainty is, the larger the gain coefficient $k_{r_{ii}}$ is, and the positive definite matrices \mathbf{K}_p and \mathbf{K}_i are related with the control system. Additionally, the calculation of $k_{r_{ii}}$ requires the determination of bounds associated with the target trajectory and the uncertainty of modeling error.

A co-simulation is performed to command the 6-MVS tracking of the acceleration spectrum, to verify the validity of the CTC-based robust PI control presented above. The amplitudes and frequencies of the co-simulation are shown in Table 3. It can be noted that the target acceleration trajectories are periodic and consist of trigonometric series of the cosine function at different

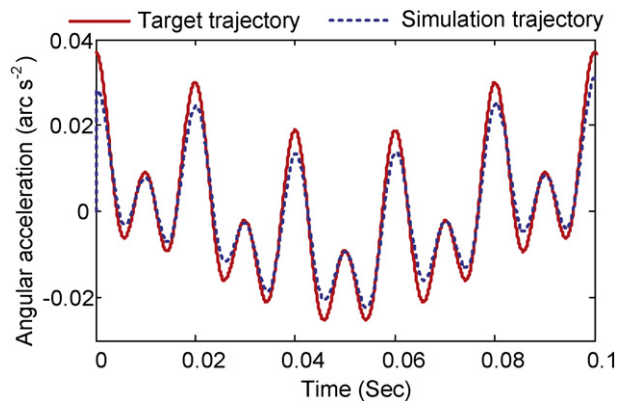


Fig. 11. Simulation result of robust PI controller with increased value.

amplitudes and frequencies. With the mass properties and stiffness coefficients are offset by 25% from the real values of the 6-MVS, the trajectory and uncertainty bounds can be computed as: $|E_{EOR,i}|_{max} = 0.8$. When the control parameters are designed as: $\mathbf{K}_i = \mathbf{K}_p = \text{diag}\{-10\}$, $\mathbf{\Lambda} = \text{diag}\{20\}$, $\mathbf{K}_r = \text{diag}\{15\}$, the simulation result of angular accelerations about the x-axis is illustrated in Fig. 10, which shows that after $t_s = 0.08\text{s}$, the control system is unstable. By changing the values of the gain matrices \mathbf{K}_i and \mathbf{K}_p , $\mathbf{K}_i = \mathbf{K}_p = \text{diag}\{100\}$, it can be observed that the control system is stable, but the angular acceleration error about z-axis is over the allowable values, which is illustrated in Fig. 11. From the theoretical analysis and simulation results, it can be concluded that the control performance of the proposed controller improves with the increase of gain matrices \mathbf{K}_i and \mathbf{K}_p . So, the control parameters are finally designed as: $\mathbf{K}_i = \mathbf{K}_p = \text{diag}\{6672\}$, $\mathbf{\Lambda} = \text{diag}\{20\}$, $\mathbf{K}_r = \text{diag}\{15\}$.

Figs. 12 and 13 show the acceleration and angular acceleration produced by the 6-MVS in the time and frequency domains, respectively. The frequency spectrum difference between the target values and outputs of the ADAMS model are given in Table 4, which shows that the frequency components of the acceleration spectrums are identical. The greatest differences in the translational acceleration amplitudes and the angular acceleration amplitudes are 2.84% and 0.18%, respectively. The smallest

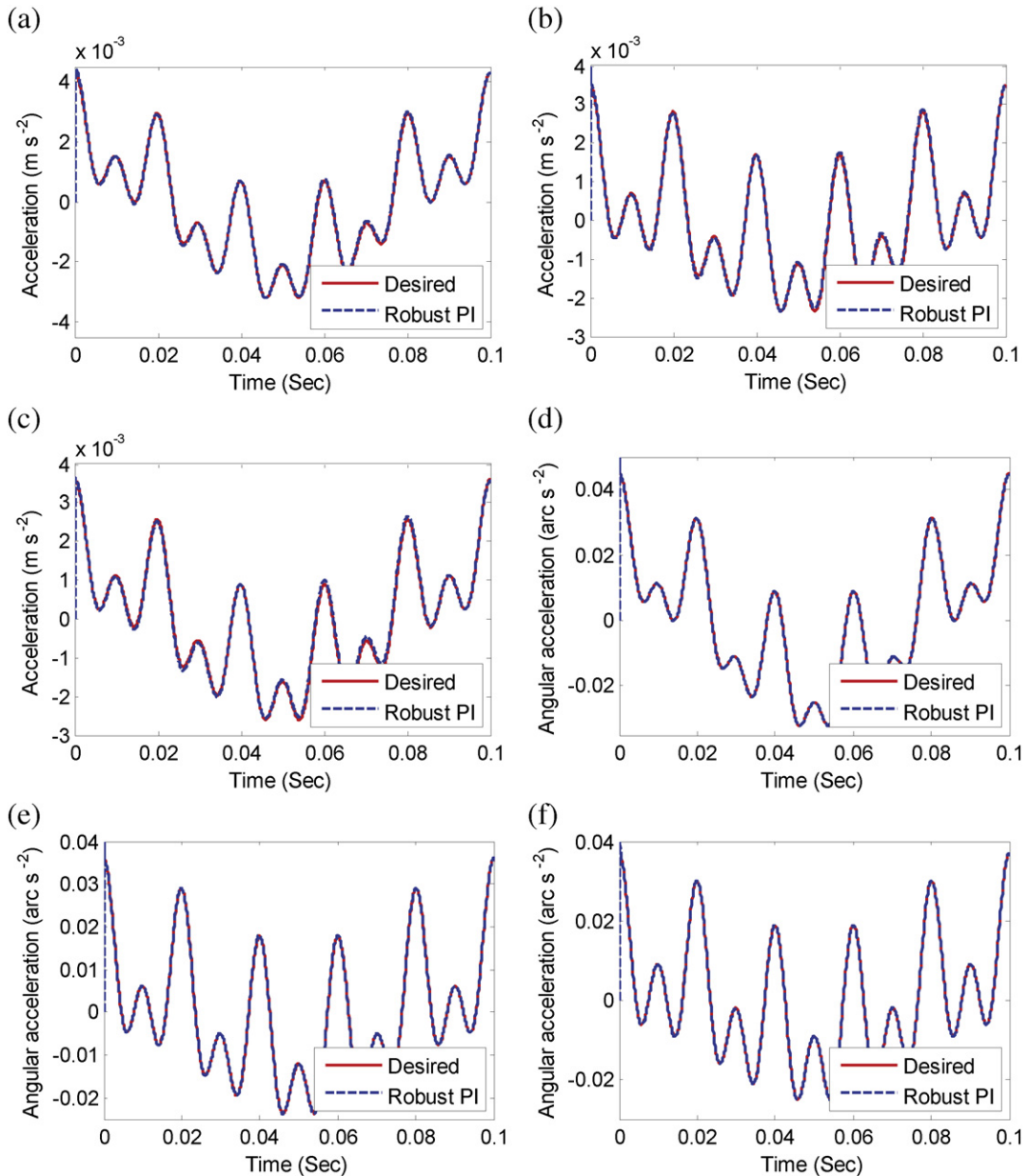


Fig. 12. Response to desired acceleration trajectories under the proposed robust PI controller in the time domain: (a) translational accelerations along the x-axis, (b) translational accelerations along the y-axis, (c) translational accelerations along the z-axis, (d) angular accelerations about the x-axis, (e) angular accelerations about the y-axis, (f) angular accelerations about the z-axis.

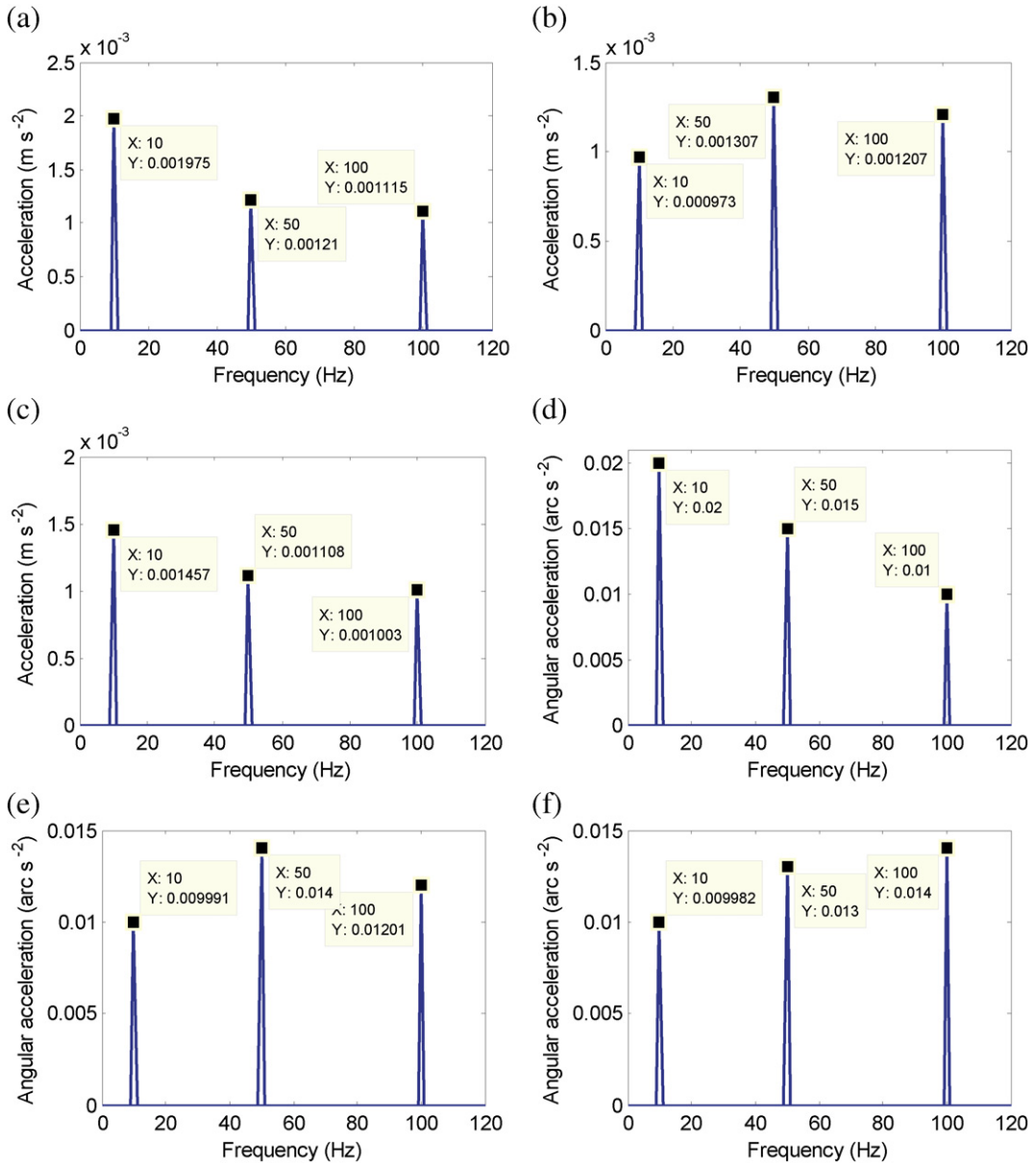


Fig. 13. Simulated acceleration trajectories in the frequency domain: translational accelerations along the x-axis, (b) translational accelerations along the y-axis, (c) translational accelerations along the z-axis, (d) angular accelerations about the x-axis, (e) angular accelerations about the y-axis, (f) angular accelerations about the z-axis.

differences in the translational acceleration amplitudes and angular acceleration amplitudes are 0.31% and 0.001%, respectively. From Fig. 11, it is clear that the acceleration spectrums generated by the simulator are consistent with the target acceleration spectrums and there is no coupling between the generated accelerations. This indicates that the micro-vibration simulator can generate the target acceleration spectrums along any arbitrary direction in the task space.

The simulation results show that the robust PI control scheme based on CTC has strong control performance even when the normal dynamic parameters of the 6-MVS deviate by 25% from the exact values. This proves that the proposed control scheme has excellent robustness and is suitable for purpose.

7. Conclusion

This study presents the structural design, inverse dynamics modeling, and robust control of a micro-vibration simulator, which can reproduce 6-DOF micro-vibrations with different amplitudes and frequencies. The Kane method is used to establish

Table 4
Frequency spectrum difference between target values and simulation values

Frequency (Hz)	Difference (%)					
	A_x	A_y	A_z	A_{rx}	A_{ry}	A_{rz}
10	1.27	2.70	2.84	0.001	0.09	0.18
50	0.85	0.54	0.71	0.001	0.02	0.001
100	1.37	0.61	0.31	0.001	0.06	0.001

a complete inverse dynamics model of the 6-DOF micro-vibration simulator (6-MVS), where the parallel manipulator is considered to be a multiple-rigid-body system. This derived dynamics model takes the effects of the flexure joint into account. The finite element method is then used to analyze the structural performance of the 6-MVS, and the model analysis results indicate that the natural frequency of the first flexible body mode is greater than 500 Hz. Additionally, a co-simulation is used to verify the validity of the inverse dynamics model, which combines ADAMS with MATLAB/Simulink. Based on the dynamics model, a robust proportional-integral controller is designed and the performances are analyzed with respect to stability, precision and robustness. The theoretical analysis and simulation results demonstrate that the proposed controller offers excellent performance for the 6-MVS. Furthermore, even when the normal dynamic parameters are offset by 25% from the real values of the 6-MVS, the 6-MVS can reproduce the target micro-vibration spectrum. This indicates that the developed solution can satisfy the initial design objectives. The design and validation methodology presented in this study can also be extended to other types of parallel manipulators.

Acknowledgments

This work was supported by the National Natural Science Foundation of China under Grant no. 11302222 and the Innovation Foundation of Changchun Institute of Optics, Fine Mechanics and Physics, Chinese Academy of Sciences under Grant no. Y4CX1SS141.

References

- [1] A.J. Bronowicki, Vibration isolator for large space telescopes, *J. Spacecr. Rockets* 43 (1) (2006) 45–53.
- [2] L. Dewell, N. Pedreiro, C. Blaurock, K.C. Liu, J. Alexander, M. Levine, Precision telescope pointing and spacecraft vibration isolation for the terrestrial planet finder coronagraph, 5899. Proceedings of SPIE, Bellingham, 2007, pp. 589902–591–14.
- [3] A.J. Bronowicki, J.W. Innis, A family of full spacecraft-to-payload isolators, *Technol. Rev. J.* 13 (2005) 21–41.
- [4] D. Kamesh, R. Pandiyan, A. Ghosal, Modeling, design and analysis of low frequency platform for attenuating micro-vibration in spacecraft, *J. Sound Vib.* 329 (17) (2010) 3431–3450.
- [5] I. Hostens, J. Anthonis, P. Kennes, H. Ramon, Six-degrees-of-freedom test rig design for simulation of mobile agricultural machinery vibrations, *J. Agric. Engng Res.* 77 (2) (2000) 155–169.
- [6] I. Hostens, J. Anthonis, H. Ramon, New design for a 6 DOF vibration simulator with improved reliability and performance, *Mech. Syst. Signal Pr.* 19 (1) (2005) 105–122.
- [7] G.Y. Park, D.O. Lee, J.H. Han, Development of multi-degree-of-freedom microvibration emulator for efficient jitter test of spacecraft, *J. Intell. Mater. Syst. Strut.* 25 (9) (2014) 1069–1081.
- [8] K.C. Liu, P. Maghami, Reaction wheel disturbance modeling, jitter analysis, and vibration, tests for solar dynamics observatory, AIAA Guidance, Navigation and Control Conference and Exhibit, Honolulu, Hawaii, 2008, 1–18.
- [9] Y.M. Li, Q.S. Xu, Dynamic modeling and robust control of a 3-PRC translational parallel kinematic machine, *Rob. Comput. Integr. Manuf.* 25 (3) (2009) 630–640.
- [10] W. Dong, Z.J. Du, Y.Q. Xiao, X.G. Chen, Development of a parallel kinematic motion simulator platform, *Mechatronics* 23 (1) (2013) 154–161.
- [11] Z.F. Shao, X.T. Tang, X. Chen, L.P. Wang, Research on the inertia matching of the Stewart parallel manipulator, *Rob. Comput. Integr. Manuf.* 28 (6) (2012) 649–659.
- [12] J. Spanos, Z. Rahman, G. Blackwood, A soft 6-axis active vibration isolator, Proceedings of the IEEE American Control Conference, Seattle, Washington, USA, 1995, 412–416.
- [13] A. Joshi, W.J. Kim, System identification and multivariable control design for a Satellite UltraQuiet Isolation Technology Experiment (SUITE), *Eur. J. Control* 10 (2) (2004) 174–186.
- [14] X.Q. Tang, Z.F. Shao, Trajectory generation and tracking control of a multi-level hybrid support manipulator in FAST, *Mechatronics* 23 (6) (2013) 1113–1122.
- [15] J.F. Yang, Z.B. Xu, Q.W. Wu, Y. Li, L.H. Chen, Y.Y. Gu, Design of six dimensional vibration isolation system for space optical payload, *Optics Precis. Eng.* 23 (5) (2015) 1347–1357.
- [16] O. Reza, M.A. Mohammad, D.T. Hamid, Explicit dynamics formulation of Stewart-Gough platform: a Newton-Euler approach, Proceedings 2010 IEEE International Conference on Intelligent Robots and Systems, Taipei, Taiwan, 2010, 2772–2777.
- [17] B. Dasgupta, T.S. Mruthyunjaya, A Newton-Euler formulation for the inverse dynamics of the Stewart platform manipulator, *Mech. Mach. Theory* 33 (8) (1998) 1135–1152.
- [18] S. Staicu, Dynamics of the 6-6 Stewart parallel manipulator, *Rob. Comput. Integr. Manuf.* 27 (2011) 212–220.
- [19] S. Staicu, Matrix modeling of inverse dynamics of spatial and planar parallel robots, *Multibody Syst. Dyn.* 27 (2012) 239–265.
- [20] H.Z. Jiang, J.F. He, Z.Z. Tong, Characteristics analysis of joint space inverse mass matrix for the optimal design of a 6-DOF parallel manipulator, *Mech. Mach. Theory* 45 (5) (2010) 722–739.
- [21] Z.Z. Tong, J.F. He, H.Z. Jiang, G.R. Duan, Optimal design of a class of generalized-free symmetric Gough-Stewart parallel manipulators with dynamic isotropy and singularity-free workspace, *Robotica* 30 (2011) 305–314.
- [22] T.X. Tian, H.Z. Jiang, Z.Z. Tong, J.F. He, Modal space decoupled optimal design for a class of symmetric spatial parallel mechanisms with consideration of passive joint damping, *Robotica* 33 (4) (2015) 828–847.

- [23] H.Z. Jiang, Z.Z. Tong, J.F. He, Dynamic isotropic design of a class of Gough-Stewart parallel manipulators lying on a circular hyperboloid of one sheet, *Mech. Mach. Theory* 46 (3) (2011) 358–374.
- [24] H.Z. Jiang, J.F. He, Z.Z. Tong, W. Wang, Dynamic isotropic design for modified Gough-Stewart platforms lying on a pair of circular hyperboloids, *Mech. Mach. Theory* 46 (9) (2011) 1301–1315.
- [25] A.F. Behrouz, L. Per, N. Kristina, Parametric damped vibrations of Gough-Stewart platforms for symmetric configurations, *Mech. Mach. Theory* 80 (2014) 52–69.
- [26] F. Paccot, N. Andreff, P. Martinet, A review on the dynamic control of parallel kinematic machines: theory and experiments, *Int. J. Robot. Res.* 28 (3) (2009) 395–416.
- [27] M. Honegger, R. Brega, G. Schweitzer, Application of a Nonlinear Adaptive Controller to a 6 DOF Parallel Manipulator, *Proceedings 2010 IEEE International Conference on Robotics and Automation*, San Francisco, 2010, 1930–1935.
- [28] D.H. Kim, J.Y. Kang, K. Lee, Robust tracking control design for 6 DOF parallel manipulator, *J. Robotic Syst.* 17 (10) (2000) 527–547.
- [29] Y. Wu, K.P. Yu, J. Jiao, R. Zhao, Dynamic modeling and robust nonlinear control of a six-DOF active micro-vibration isolation manipulator with parameter uncertainties, *Mech. Mach. Theory* 92 (2015) 407–435.
- [30] C.F. Yang, Q.T. Huang, J.W. Han, Computed force and velocity control for spatial multi-DOF electro-hydraulic parallel manipulator, *Mechatronics* 22 (6) (2012) 715–722.
- [31] C.F. Yang, Q.T. Huang, J.W. Han, Decoupling control for spatial six-degree-of-freedom electro-hydraulic parallel robot, *Rob. Comput. Integr. Manuf.* 28 (1) (2012) 14–23.
- [32] C.F. Yang, Q.T. Huang, H.Z. Jiang, O.O. Peter, J.W. Han, PD control with gravity compensation for hydraulic 6-DOF parallel manipulator, *Mech. Mach. Theory* 45 (4) (2010) 666–677.
- [33] C.F. Yang, J.F. He, J.W. Han, X.C. Liu, Real-time state estimation for spatial six-degree-of-freedom linearly actuated parallel robots, *Mechatronics* 19 (6) (2009) 1026–1033.
- [34] H.B. Guo, Y.G. Liu, G.R. Liu, H.R. Li, Cascade control of a hydraulically driven 6-DOF parallel robot manipulator based on a sliding mode, *Control Eng. Pract.* 16 (9) (2008) 1055–1068.
- [35] H.S. Kim, Y.M. Cho, K. Lee, Robust nonlinear task space control for 6 DOF parallel manipulator, *Automatica* 41 (9) (2005) 1591–1600.
- [36] M. Stehman, N. Nakata, Direct acceleration feedback control of shake tables with force stabilization, *J. Earthquake Eng.* 17 (2013) 736–749.
- [37] N. Nakata, Acceleration trajectory tracking control for earthquake simulators, *Eng. Struct.* 32 (8) (2010) 2229–2236.
- [38] A. Preumont, M. Horodincu, I. Romanescu, B. Marneffe, M. Avraam, A. Deraemaeker, F. Bossens, A.A. Hanieh, A six-axis single-stage active vibration isolator based on Stewart platform, *J. Sound Vib.* 300 (2007) 644–661.
- [39] B. Marneffe, M. Avraam, A. Deraemaeker, M. Horodincu, A. Preumont, Vibration isolation of precision payloads: a six-axis electromagnetic relaxation isolator, *J. Guid. Control Dynam.* 32 (2) (2009) 395–401.